Nano-Materials and Electronic Devices

RLE Group
Nano-Materials and Electronics Group

Academic and Research Staff
Professor Jing Kong

Visiting Scientists and Research Affiliates
Dr. Sreekar Bhaviripudi, Dr. Ya-Ping Hsieh, Dr. Ki Kang Kim, Dr. Tingying (Helen) Zeng

Visiting Students
Ms. Xiaoling Shi, Mr. Yumeng Shi, Mr. Kai Zhang

Graduate Students
Ms. Hootan Farhat, Mr. Mario Hofmann, Mr. Allen L. Hsu, Mr. Kyeong-Jae Lee, Mr. Daniel Nezich, Mr. Hyesung Park, Mr. Alfonso R. Reina Cecco

Technical and Support Staff
Ms. Laura M. von Bosau

Group Overview
The RLE Nano-Materials and Electronics Group pursues investigations of carbon nanotubes, including studies of chemical vapor deposition methods, electron transport in single-walled carbon nanotubes, nanotube synthesis, and tunable Raman systems for characterizing the chirality of nanotube materials. A major objective of the group is to develop synthesis and control techniques to create electronic devices based on carbon nanotubes.

1. Engineering Polycrystalline Ni Films To Improve Thickness Uniformity of the Chemical-Vapor-Deposition-Grown Graphene Films

Sponsors

Project Staff
Stefan Thiele, Alfonso Reina, Paul Healey, Jakub Kedzierski, Peter Wyatt, Pei-Lan Hsu, Craig Keast, Juergen Schaefer, and Jing Kong

During the past few years research in graphene has caught a lot of attention due to its remarkable properties, such as high electron and hole mobility ($\sim$up to 200,000 cm^2 V^{-1} s^{-1}) [1], high current carrying capability (up to 3 $\times10^8$ A cm^{-2}) [2] and high mechanical robustness [3, 4]. Many potential applications have been proposed [5–8] and, as a result, it is highly desirable to develop reliable synthesis techniques to fabricate the graphene material. Recently we have developed a facile method to grow few-layer graphene films by atmospheric pressure chemical vapor deposition (CVD) using Ni thin films deposited on SiO$_2$/Si substrates [9–11]. Comparing with previous methods to grow graphene flakes/films on metallic substrates, one significant advantage is that the thin Ni film on top of the SiO$_2$/Si substrate develops a flat surface and eliminates the need of any surface polishing. The high temperature annealing step gives rise

to a polycrystalline Ni film which has single-crystal grains with atomically flat terraces. The growth of high quality, few-layer graphene on the Ni film is enabled and afterwards the Ni film can be easily etched away so that the graphene film can be transferred to another substrate. These Ni films are deposited onto SiO$_2$/Si substrates by sputtering. Depending on the sputtering conditions (substrate temperature, chamber pressure, etc), different average sizes of the Ni grains were obtained after the high temperature annealing. In this work, we investigated the influence of the Ni grain sizes on the morphology of the CVD-grown graphene. It was found that, under present CVD growth conditions, one or two layers of graphene grow on top of the flat single-crystal grains and multilayer graphene usually grows at the grain boundary regions. Therefore there is a close correlation between the grain size distributions of the Ni films with the morphology of the graphene films. Obtaining large grains in the Ni film is more favorable in minimizing the thickness non-uniformity of the graphene film. Previous understanding on the grain growth in transition metal films provides significant guidance in finding the optimum conditions of the Ni film deposition and annealing to obtain large Ni grain sizes which favor the growth of 1–2-layer graphene regions.

Our graphene growth starts with Ni-coated SiO$_2$/Si substrates; the Ni thin film is deposited by sputtering to a thickness of 500 nm. In a typical growth, the substrate is loaded into a quartz tube and heated up in a CVD furnace to 900–1100°C. This annealing process is carried out under H$_2$ and Ar atmosphere. The flow rate is kept constant at 200 sccm and 800 sccm for H$_2$ and Ar, respectively. Afterwards we either stay at the same furnace temperature or change to a different temperature to start the graphene growth. In the CVD growth step we change the flow rate of H$_2$ to 1300 sccm and stop introducing Ar. Simultaneously we start flowing ~4 sccm CH$_4$, which acts as the carbon source. After 5 min of growing we take the quartz tube out of the furnace and cool it down under H$_2$ and Ar.

In the Ni grain growth experiments, we only carried out the annealing step before cooling the substrate to room temperature.

Evolution of the Ni film and correlation between the Ni structure and graphene thickness variation. Figure 1 shows the evolution of the Ni film surface at different stages during the graphene synthesis process. Figure 1(a) is an AFM image of the Ni surface after sputter deposition. Compared with the underlying SiO$_2$/Si substrate, the surface became rougher. The RMS value increased from 0.163 (thermal SiO$_2$) to 4.40 nm (sputtered Ni). During the annealing process some of the nickel grains start to grow whereas the others shrink. This growing process can be described by the following equation [12]:

$$dr/dt = M\left[\left(\overline{\gamma}_s - \gamma_s/h\right) + \left(\overline{\gamma}_i - \gamma_i/h\right) + \gamma_{gb}\left(1/\overline{r} - 1/r\right)\right] \tag{1}$$

where r is the grain radius, $\overline{r}$ is the average grain radius, M is the grain boundary mobility, γ_s is the surface energy, $\overline{\gamma}_s$ is the average surface energy, γ_i is the interface energy (to the substrate), $\overline{\gamma}_i$ is the average interface energy, γ_{gb} is the grain boundary energy and h is the film thickness. If dr/dt >0 the grain starts to grow, otherwise it will shrink. Therefore the growth of a grain with the surface/interface energy slightly smaller than the average surface/interface energy will be promoted. As a result, some grains grow whereas other grains will vanish. The average grain size increases during the annealing. This result is shown in Figure 1(b), which is an optical image of the surface of the nickel film after 20 min of annealing at 900°C. The black lines are the Ni grain boundaries. The lateral size of the grains after annealing can be as large as tens of μms. Each grain is a single-crystal grain with a flat surface [Figure 1(d)]. The RMS roughness is 1.38 nm. The grains are separated by groove-like grain boundaries, which can be deeper than 30 nm.
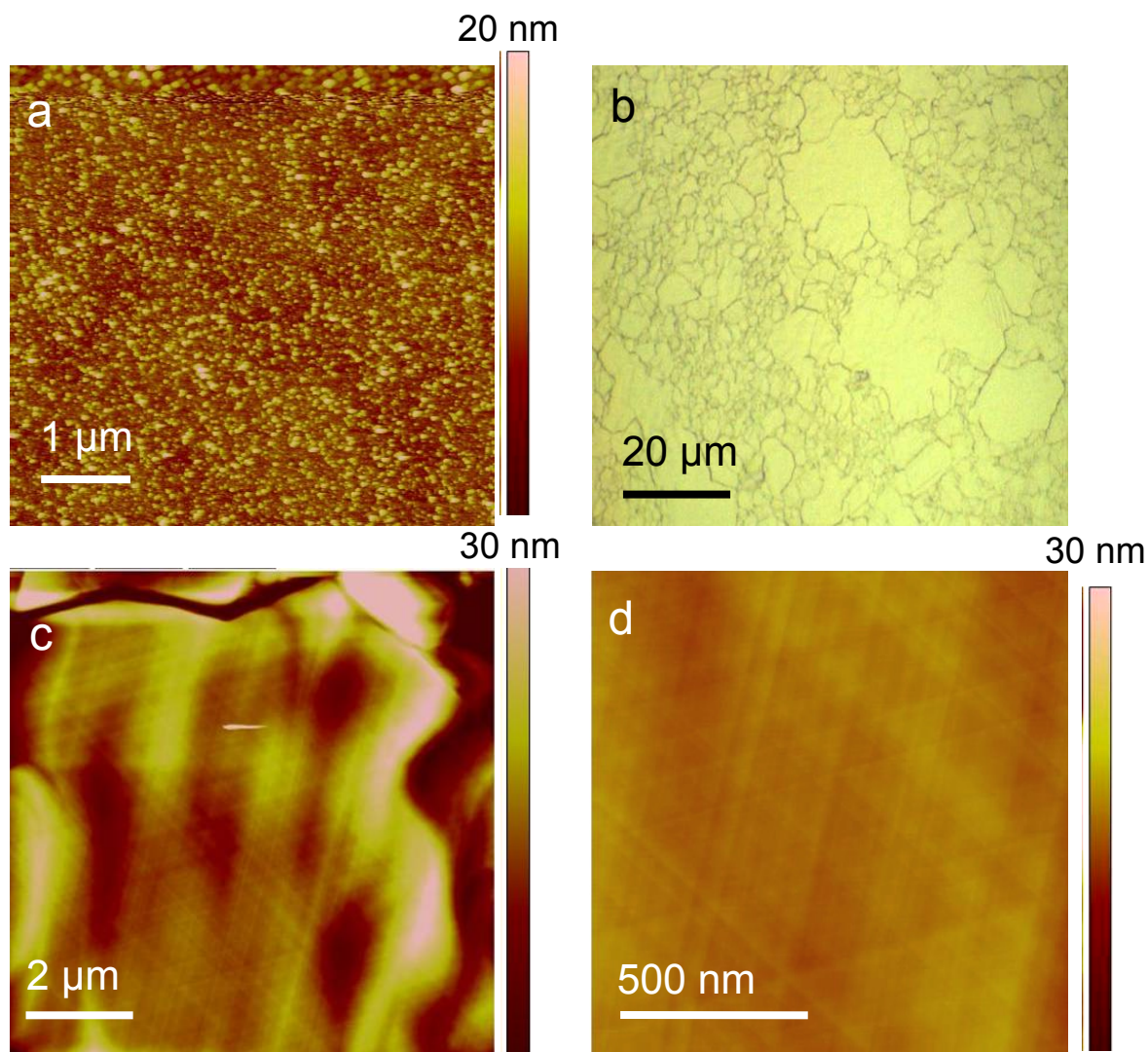
Figure 1. The Ni surface morphology before the CVD growth of graphene. (a) AFM image of Ni surface after deposition, but before annealing. (b) Optical image of the Ni film after annealing under H2 environment before CVD synthesis. (c) AFM image of the Ni film surface after annealing, showing both the grains and grooves at the grain boundaries. (d) AFM image of the surface of a single grain showing the flat surface.

In Figure 2(a) the optical image of an as-grown sample surface is shown. The darker areas near the grain boundaries correspond to graphite whereas on top of the nickel grains we get one or two layers of graphene. We see the correlation between the sizes of the nickel grains and the sizes of the graphene areas with one or two graphene layers in Figures 2(b) and (c) (see circled areas). The 1–2-layer graphene area is limited by the size of the nickel grains. Therefore in order to enlarge these 1–2-layer regions it is necessary to increase the size of the nickel grains. This leads to our following investigations towards a better understanding of the growth mechanism of the nickel grains on SiO_2.
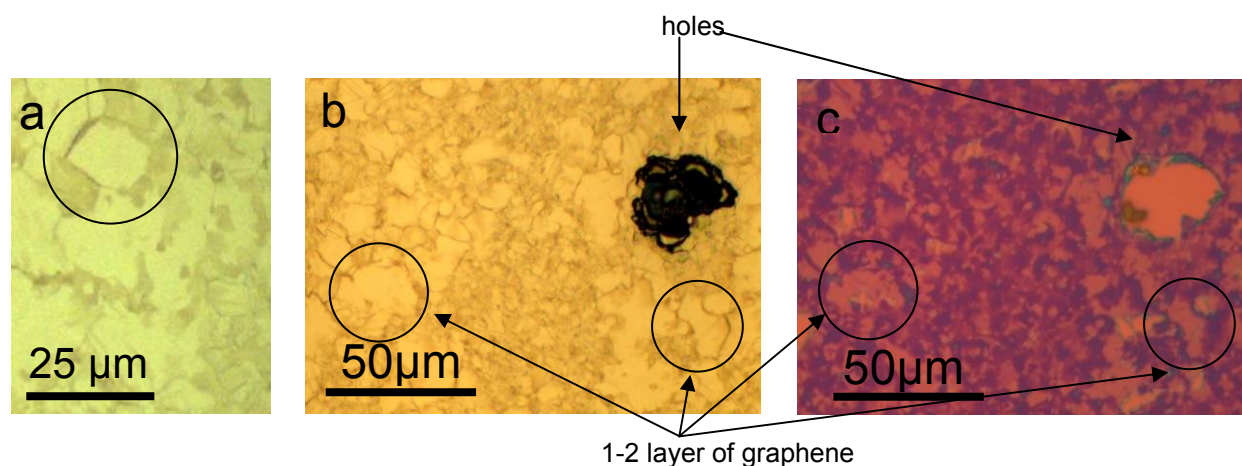
Figure 2. The correlation of the Ni grain structure and the thickness variation of the graphene film on top of the Ni film. (a) Optical image of the Ni surface with graphene after CVD growth; the black lines are the grain boundaries between Ni grains and the darker regions correspond to multilayer graphene [the thin graphene layers cannot be seen in this image, but are situated on top of the single-crystal nickel grains (circled area)]. (b) Optical image of a graphene film on Ni at a location with one hole in the Ni film which is used as a marker. (c) Optical image of the same graphene region transferred to the SiO$_2$/Si substrate showing a direct correlation of the graphene film thickness variation with the grain structure of the Ni film.

Controlling Ni grain growth. Reducing thermal stress inside the Ni film. In general there are two different types of grain growth [12], which are normal and abnormal grain growth. An important characteristic of the normal grain growth is that, after the annealing, the average grain size does not exceed the film thickness. Also the shape of the grain size distribution of the single grains is not changing. Only the peak of the distribution shifts to larger grain sizes. Normal grain growth rarely occurs in thin films. Abnormal grain growth is preferred: due to the surface and interface energy anisotropy, only a subpopulation of the grains which are favored will start to grow. Therefore the grain size distribution develops until the portion of the population which is not favored is eliminated. The abnormal grain growth has the characteristic that the average grain size is up to an order of magnitude larger than the film thickness.

In our experiments we used 500 nm sputtered Ni films. This implies that our grains should also be in the range of several hundred nanometers if we observe normal grain growth. However, they were much bigger in our experiments. The ratio of the grain diameter (about 10 μm) to the thickness of the nickel film (500 nm) is around 20 which could only be obtained by abnormal grain growth [12]. In the case of abnormal grain growth, the driving forces are the surface/interface energy minimization or stress minimization [12]. In fcc metals, the (111) planes always have the lowest surface/interface energy with respect to other crystallographic orientations [13]. Therefore the growth of Ni(111) grains (i.e., grains having their surface normal perpendicular to the (111) crystal plane) is preferred due to energy minimization between the Ni(111) surface and the underlying substrate. However, in the case of Ni films having high stress, the surface/interface energy minimization is no longer the dominant driving force. Rather, the system tries to minimize its internal stress instead of the surface/interface energy. In this case, the growth of grains with a (100) crystallographic orientation is preferred because the Young's modulus has the lowest value in the (100) direction for fcc metals—in order to reduce the internal stress, Ni(100) grains are easier to expand or compress than grains with other orientations. In order to grow graphene epitaxially on nickel, the lattice mismatch should be small. The smallest mismatch is for grains with the (111) orientation (1.2%). Therefore we optimized the nickel film to promote the growth of (111) grains. The total stress depends on the thickness of the film and on the difference between the deposition temperature and the annealing (grain growth) temperature, ΔT [14]. As a result, the amount of stress in

the nickel film determines the type of energy minimization in the Ni film and therefore the grain orientations that are favored during grain growth. The total stress σ_{total} in the nickel film can be calculated by the following formula:

$$\sigma_{total} = \sigma_{thermal} + \sigma_{intrinsic} + \sigma_{external} \qquad (2)$$

where $\sigma_{thermal}$ is the stress which occurs during annealing due to the different expansion coefficients of Si and Ni and $\sigma_{external}$ is the stress which is caused by an external force. The stress at room temperature when no external force is applied is $\sigma_{intrinsic}$. In our experiment we can neglect $\sigma_{external}$, because there is no external force. In the case when $\sigma_{total} > 0$ we speak of tensile stress, otherwise it is compressive stress. The thermal stress is given by the following expression:

$$\sigma_{thermal} = (\alpha_{Si} - \alpha_{Ni})(T_{annealing} - T_{deposition}) \qquad (3)$$

This means the higher the temperature difference ΔT $(=T_{annealing} - T_{deposition})$ the higher the thermal stress. Therefore during the grain growth, the system will favor energy minimization with low ΔT (i.e., low $\sigma_{thermal}$) and will favor stress minimization under high ΔT (i.e., high $\sigma_{thermal}$). Due to the fact that $\alpha_{Si} < \alpha_{Ni}$ and $T_{deposition} < T_{annealing}$ the stress at the annealing temperature of 1000°C is highly compressive. In order to enhance the growth of Ni(111) grains we need to decrease ΔT and therefore increase $T_{deposition}$. Similar conclusions have been made by investigations in Ag film growth, which is also an fcc metal as Ni [14]. Thus we used higher deposition temperatures to minimize the stress. In order to confirm that we really promoted the growth of grains with (111) morphology with respect to grains with (100) morphology or other crystallographic directions, we carried out x-ray diffraction analysis (see Figure 3). Before we annealed our samples, the Ni films contained grains with both (111) and (100) orientations. After the annealing, only the (111) diffraction peak was detected, suggesting an increase in the population of Ni(111) grains.
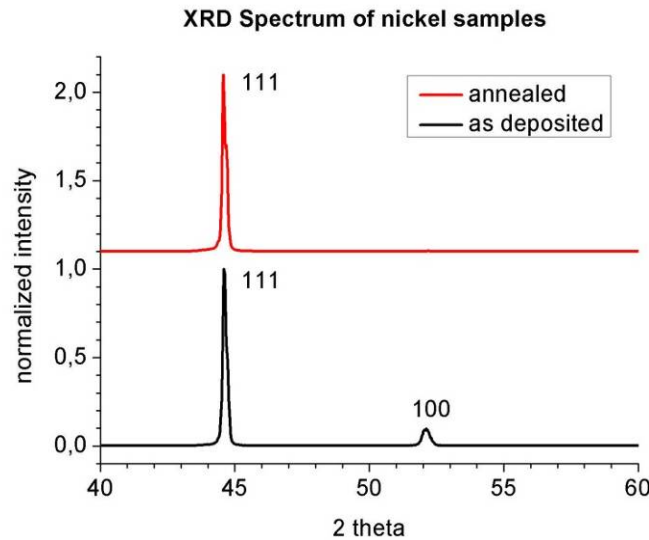

Figure 3. XRD data of the nickel thin film before annealing (black) and after annealing (red). The intensity is normalized to the nickel (111) peak. The red curve has an arbitrary offset in the *y* direction for better illustration.

We found that a positive side effect of minimizing the stress in the system was that the nickel grains grow larger under lower stress, which results in larger areas of one-or two-layer graphene. The optical images for three different deposition temperatures are illustrated in Figure 4. We used the Image J software to

obtain an estimate of the average grain sizes. It shows that we obtained the largest nickel grains for the higher deposition temperature (450°C).
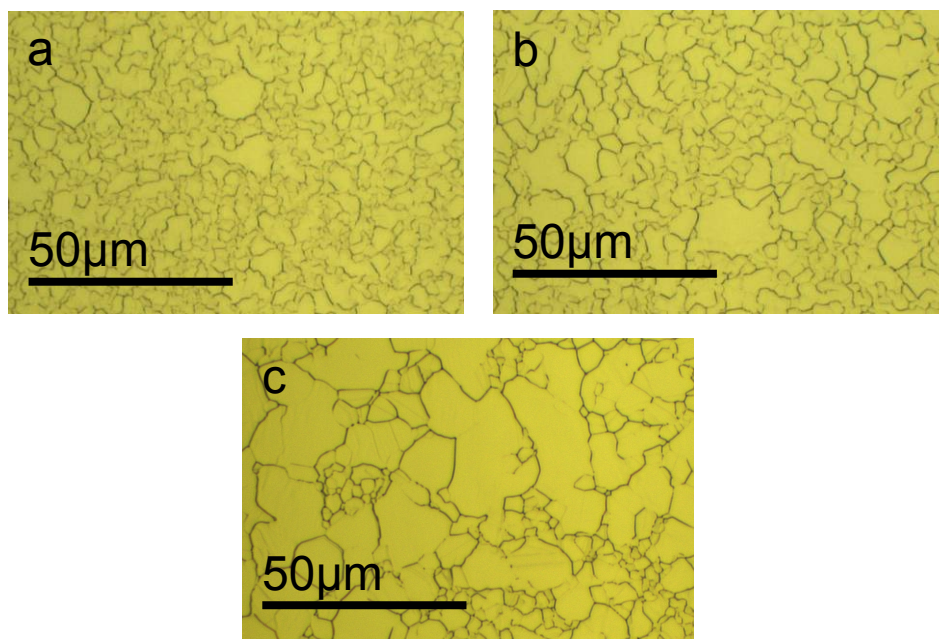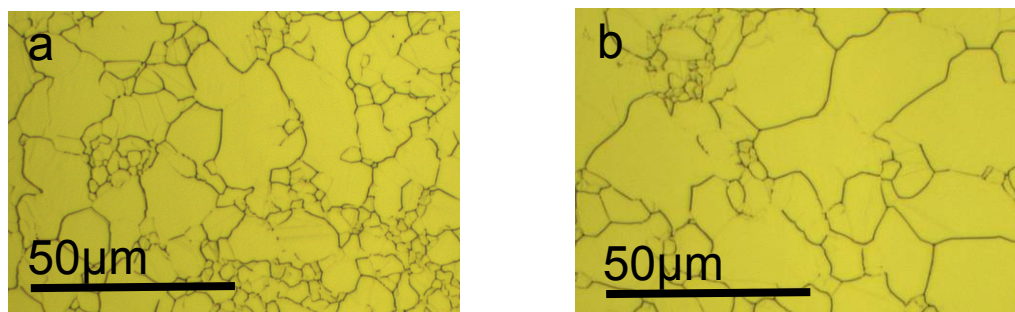

Figure 4. The optical images of 500 nm thick polycrystalline nickel films are displayed for different deposition temperatures: (a) (50°C), (b) (350°C) and (c) (450°C). They are all annealed under the same conditions.

Reducing the internal stress. The deposition conditions were also optimized to decrease the stress in the film and enhance grain growth. Since the limit of the deposition temperature (determined by our deposition chambers) was reached, we started to manipulate the intrinsic stress. As the thermal stress is compressive in our experiments, a tensile intrinsic stress would help to decrease the total stress in the film.

One way to do this is by increasing the argon pressure during sputtering deposition. The intrinsic stress (tensile) increases monotonically with argon pressure [15].

In Figure 5 we compared two 500 nm thick nickel films sputtered at 3 mT and 15 mT argon pressure, respectively. They are both annealed at the same conditions. This experiment confirms the previous understanding. The sample with the lower total stress (high argon pressure) shows larger nickel grains.


Figure 5. Optical images of the surface of a 500 nm thick nickel film after the annealing. (a) Deposition temperature: 450°C, argon pressure: 3 mT; (b) deposition temperature: 450°C, argon pressure: 15 mT.

Effect of the underlying surface. Apart from tailoring the sputtering condition to get large grains in the (111) orientation, we also observed an interesting effect on the grain growth by the underlying SiO_2 surface. We sputtered Ni under the same conditions onto three different types of SiO_2 substrates: thermally grown SiO_2, low stress PECVD-grown SiO_2 and PECVD-grown SiO_2. Figure 6 shows that the size of the nickel grains is smallest on the thermally grown SiO_2 and is largest on PECVD-grown SiO_2. All three samples were annealed under the same conditions. The grain size of polycrystalline nickel on PECVD SiO_2 is a factor of 2 larger than on thermally grown SiO_2. At present the exact reason for this interface effect is not known; one possibility is the difference in the roughness of the surfaces.
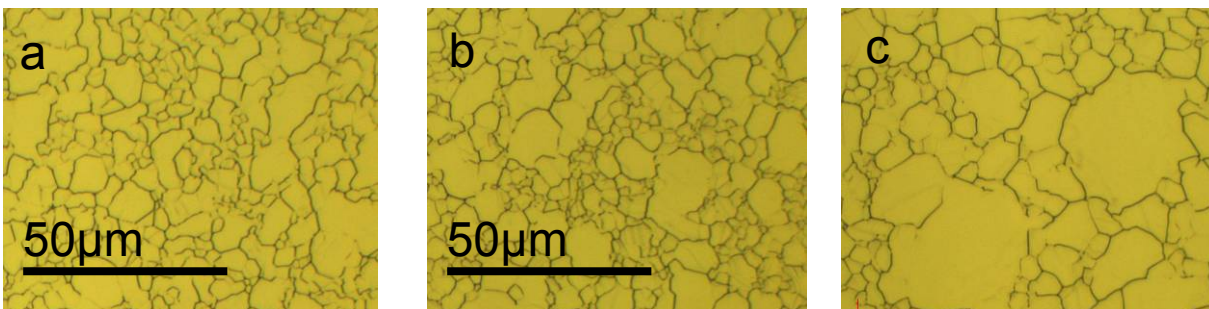
Figure 6. Optical image of the annealed 500 nm thick nickel film on top of thermally grown SiO_2 (a), low stress PECVD SiO_2 (b) and PECVD SiO_2 (c).

Figure 7 shows the AFM images of these three types of substrates. The arithmetic average roughnesses are 0.163 nm, 1.33 nm and 1.4 nm for thermal SiO_2, low stress PECVD SiO_2 and PECVD SiO_2, respectively. Since the interface with the highest roughness has the largest area, which will give rise to the largest surface/interface energy, it is possible that, due to this reason, the PECVD SiO_2 promotes the largest grain growth of the Ni film among the three types of substrates.
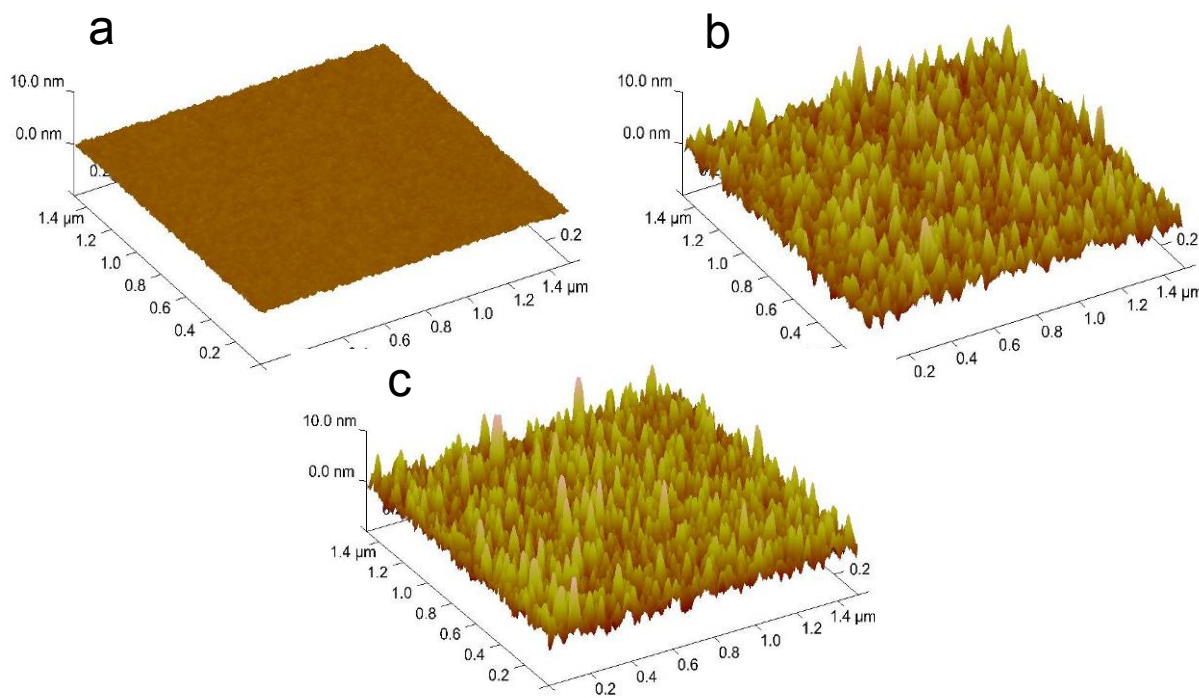

Figure 7. The AFM images of thermally grown SiO_2 (a), low stress PECVD grown SiO_2 (b) and PECVD-grown SiO_2 (c) are displayed. Their arithmetic average roughness values are 0.163 nm, 1.33 nm and 1.4 nm for thermal SiO_2, low stress PECVD SiO_2 and PECVD SiO_2, respectively.

Time dependence. Another way to increase the grain size of the nickel grains is by optimizing the annealing process. There are two very important equations which describe the grain growth in a certain range:

$$r \propto \sqrt{\alpha t} \tag{4}$$

$$\alpha = \alpha_0 e^{\frac{Q}{kT}}, \tag{5}$$

where *r* is the grain radius, α is the grain boundary mobility, *t* is the annealing time, *Q* is the activation energy for the grain boundary motion, *k* is the Boltzmann constant and *T* is the annealing temperature. It should be noticed that these equations hold only for an ideal case. In reality the grain growth becomes stagnant. During the grain growth a groove is forming at the grain boundary. When the groove becomes deeper the curvature of the grain boundary increases. If this curvature exceeds a certain threshold, the grain boundary motion stops and the grain growth stagnates [16]. We did some experiments to check for this dependence. Figure 8 shows the first experiment where we took a nickel sample and changed the annealing time, leaving everything else constant. It is noticeable that with increasing annealing time the grain size is increasing. Notice that there is a large change in the average grain size between 1 and 15 min of annealing, but only a small change between 15 and 40 min of annealing. This is due to the stagnation of grain growth.
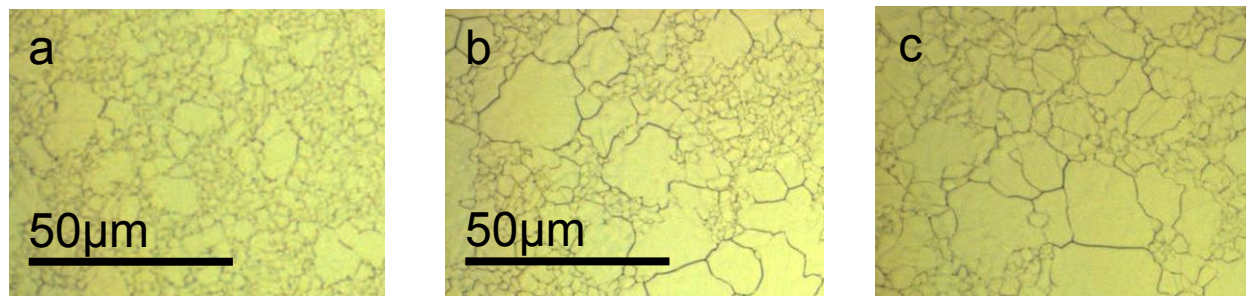

Figure 8. The optical image of the polycrystalline nickel surface after an annealing time of 1 min (a), 15 min (b) and 40 min (c). The annealing temperature is 1000°C.

When we expose a thin nickel film to H_2 under elevated temperatures we observe that the nickel starts to vanish at different spots ["holes" in the Ni film, such as the one shown in Figure 2(b)]. Under elevated temperatures hydrogen atoms are able to diffuse into the nickel and form hydrogen clusters. These clusters grow over time and build up pressure. If the pressure overcomes the cohesive force in the nickel, cracks will initiate at the walls of these clusters and destroy the nickel film [15]. The resulting pinholes are called hydrogen blisters. Their amount increases with longer annealing times and higher annealing temperatures. The presence of the holes complicates the graphene growth and transfer process and is thus undesirable. As a result, there is an optimum time for our Ni film annealing.

Temperature dependence. In the next step we checked the dependence of the grain size on the annealing temperature. Three samples were annealed at 900°C, 1000°C and 1100°C, respectively. The annealing time in all three experiments was only 1 min. The result of this experiment is displayed in Figure 9. The strong increase of the grain size with increasing temperature is clearly noticeable.
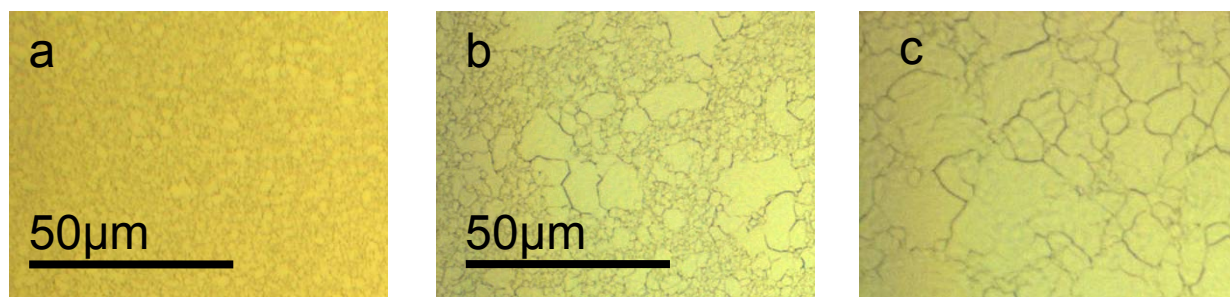
Figure 9. Optical images of the surface of the nickel film which was annealed for one minute at (a) 900°C, (b) 1000°C, and (c) 1100°C.

The short annealing time in this experiment avoids damage of the 500 nm thick nickel film by hydrogen blisters. After combining the two main results of the previous experiments (i.e., optimizing the film deposition conditions in terms of substrate temperature and Ar gas pressure during deposition; long annealing times lead to successive damage of the nickel film and high temperatures for enhanced grain growth velocity) we came up with an optimized annealing procedure. The most important part of this annealing procedure is to heat up the sample very fast to high temperatures and to stay there only for a short time period. Afterwards we cool down the sample to the temperature that is needed for the following CVD process. The sketch of the annealing procedure is illustrated in Figure 10.
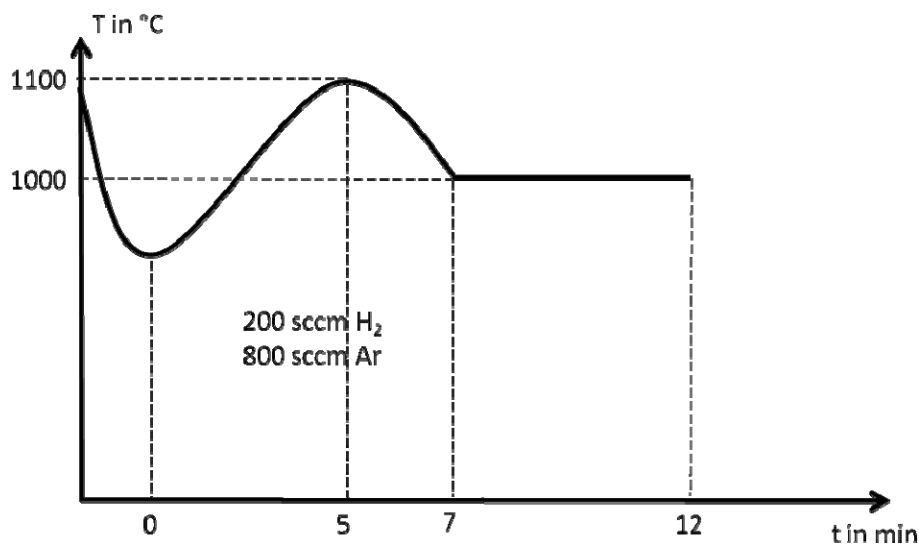
Figure 10. Illustration of the optimized annealing procedure. It takes only 7 min and starts with a ramp up to 1000°C followed by a cool down to 1000°C, which is necessary to avoid the destruction of the nickel film.

The curve shows that the furnace is preheated to 1100°C in order to save time. As the CVD tube containing the sample is introduced, the temperature drops. Afterwards the sample is heated in a very short time to 1100°C. As soon as the sample reaches this temperature, the furnace is cooled down to 1000°C. This process gave the largest average grain size without significant damage of the nickel film. We also reduced the amount of H_2 as much as possible, because of the negative effect of H_2 on the nickel film. However, the introduction of some H_2 flow was still necessary to avoid oxidation of the Ni film at high temperatures and preserve the catalytic activity of the Ni surface during the CVD process.

After optimizing the grain growth we were able to increase the thickness uniformity of the graphene significantly. The results are shown in Figure 11.
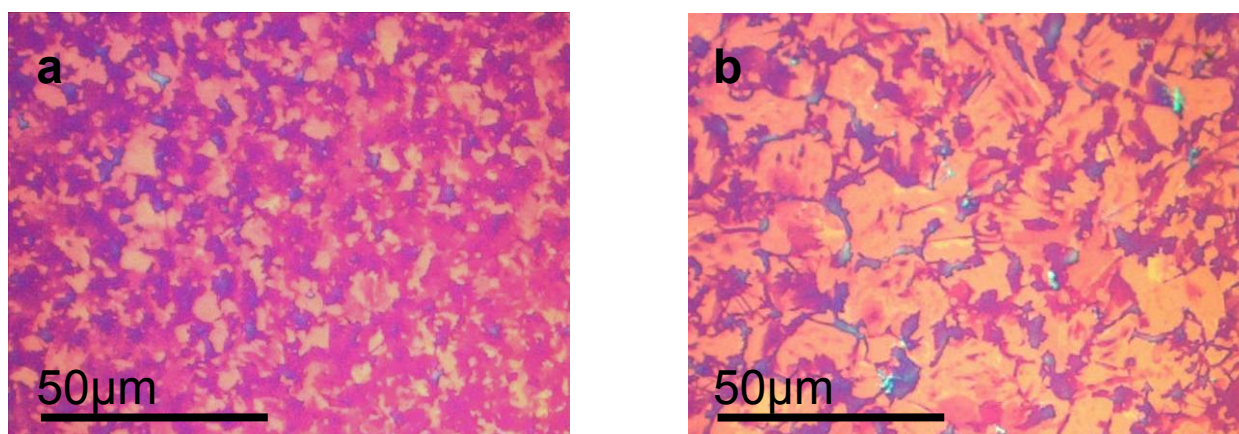
Figure 11. Optical image of the transferred graphene using an unoptimized Ni film (a) and optimized Ni film (b) of the nickel grain growth.

In summary, we introduced different procedures to obtain very large grains in a thin nickel film with (111) orientation, in order to improve the thickness uniformity of the graphene grown from these Ni films. We have shown that a high deposition temperature and a high argon pressure promotes the growth of nickel grains with (111) orientations and also increases the grain size itself. A rough surface enhances the driving force of the abnormal grain growth and thus results in large grain sizes. Based upon these understandings, we developed an annealing procedure which uses high temperatures and short annealing times to grow larger nickel grains without any destruction of the surface due to hydrogen blisters.

References

[1] S. V. Morozov, K. S. Novoselov, M. I. Katsnelson, F. Schedin, D. C. Elias, J. A. Jaszczak, and A. K. Geim, "Giant Intrinsic Carrier Mobilities in Graphene and Its Bilayer" *Physical Review Letters* **100(1):** 016602 1-4 (2008).

[2] J. Moser, A. Barreiro, and A. Bachtold, "Current-Induced Cleaning of Graphene," *Applied Physics Letters* **91(16):** 163513 1-3 (2007).

[3] J. S. Bunch, A. M. van der Zande, S. S. Verbridge, I. W. Frank, D. M. Tanenbaum, J. M. Parpia, H. G. Craighead, and P. L. McEuen, "Electromechanical Resonators from Graphene Sheets," *Science* **315(5811):** 490-493 (2007).

[4] C. Lee, X. Wei, J. W. Kysar, and J. Hone, "Measurement of the Elastic Properties and Instrinsic Strength of Monolayer Graphene," *Science* **321(5887):** 385-388 (2008).

[5] P. Blake, P. D. Brimicombe, R. R. Nair, T. J. Booth, D. Jiang, F. Schedin, L. A. Ponomarenko, S. V. Morozov, H. F. Gleeson, E. W. Hill, A. K. Geim, and K. S. Novoselov, "Graphene-Based Liquid Crystal Device," *Nano Letters* **8(6):** 1704-1708 (2008).

[6] G. Eda, G. Fanchini, and M. Chhowalla, "Large-Area Ultrathin Films of Reduced Graphene Oxide as a Transparent and Flexible Electronic Material," *Nature Nanotechnology* **3(5):** 270-274 (2008).

[7] F. Schedin, A. K. Geim, S. V. Morozov, E. W. Hill, P. Blake, M. I. Katsnelson, and K. S. Novoselov, "Detection of Individual Gas Molecules Absorbed on Graphene," *Nature Materials* **6(9):** 652-655 (2007).

[8] X. Wang, L. J. Zhi, and K. Mullen, "Transparent, Conductive Graphene Electrodes for Dye-Sensitized Solar Cells," *Nano Letters* **8(1):** 323–327 (2008).

[9] K. S. Kim, Y. Zhao, H. Jang, S. Y. Lee, J. M. Kim, K. S. Kim, J-H. Ahn, P. Kim, J-Y. Choi, and B. H. Hong, "Large-Scale Pattern Growth of Graphene Films for Stretchable Transparent Electrodes," *Nature* **457(7230):** 706-710 (2009).

[10]   A. Reina, X. Jia, J. Ho, D. Nezich, H. Son, V. Bulovic, M. S. Dresselhaus, and J. Kong, "Large-Area, Few-Layer Graphene Films on Arbitrary Substrates by Chemical Vapor Deposition," *Nano Letters* **9(1):** 30-35 (2009).

[11]   Q. Yu, J. Lian, S. Siriponglert, H. Li, Y. P. Chen, and S-S. Pei, "Graphene Segregated on Ni Surfaces and Transferred to Insulators," *Applied Physics Letters* **93(11):** 113103 1-3 (2008).

[12]   C. V. Thompson, "Grain Growth in Thin Films," *Annual Review of Materials Science* **20:** 245-268 (1990).

[13]   R. Carel, C. V. Thompson, and H. J. Frost, "Computer Simulation of Strain Energy Effects VS Surface and Interface Energy Effects on Grain Growth in Thin Films," *Acta Materialia* **44(6):** 2479-2494 (1996).

[14]   C. V. Thompson and R. Carel, "Stress and Grain Growth in Thin Films," *Journal of the Mechanics and Physics of Solids* **44(5):** 657-673 (1996).

[15]   IMAPS Flip Chip Technology Workshop, Austin, Texas, June 15-18, 2003.

[16]   W. W. Mullins, "The Effect of Thermal Grooving on Grain Boundary Motion," *Acta Metallurgica* **6(6):** 414-427 (1958).

2.   Growth of Large-Area Single- and Bi-Layer Graphene By Controlled Carbon Precipitation on Polycrystalline Ni Surfaces

Project Staff

Alfonso Reina, Stefan Thiele, Xiaoting Jia, Sreekar Bhaviripudi, Mildred S. Dresselhaus, Juergen A. Schaefer, and Jing Kong

Exploring ways to synthesize graphene which allow scalability, have low fabrication cost and facilitate integration with other materials, could play an important role in both fundamental research and the realization of future graphene applications. Several graphene synthesis approaches have been developed, including: (1) exfoliation methods (both mechanical [1, 2] and chemical [3–8]); (2) graphitization of SiC surfaces [9, 10]; (3) graphene precipitation/deposition on transition metal surfaces [11, 12]; (4) gas phase/substrate-free formation of graphene sheets [13]. Procedures such as (1) and (4) produce free-standing graphene isolated from any substrate which enables the integration of graphene with other materials. Methods like (2) and (3) produce graphene bound to a specific substrate which limits the flexibility of these approaches. Recently, it has been shown that graphene films can be grown by ambient pressure chemical vapor deposition (CVD) on thin films of transition metals and isolated from their growth substrate [14–16]. This approach is promising for generating large scale graphene on a wide range of substrates. However, these films vary in thickness from 1 to ~10 layers across their area [14–16, 17]. Here, we present an important advance to further improve the thickness uniformity of these films. We show that the area of multilayer graphene regions on the film can be reduced and the regions with single- or bi-layer graphene (1–2 LG) can be increased to 87% of the overall film area.

The precipitation of monolayer and multilayer graphene from bulk transition metals is widely known [18, 19]. It occurs due to the temperature-dependent solubility of carbon in transition metals. This concept has

recently been used to produce 1–2 LG under either vacuum conditions [11, 19] or in an ambient pressure CVD process [14–17]. In our process, carbon is introduced into the bulk of thin (~500 nm) Ni films by decomposing a highly diluted hydrocarbon gas (CH_4). Graphene precipitation is promoted on the surface of the Ni films upon cooling of the Ni–C solid solution. A summary of the three-stage process that is utilized is shown in Figure 1. The samples are heated to 900°C and annealed for 20 min at this temperature (stage 1) under Ar and H_2 in order to smooth the Ni surface and to activate Ni grain growth.
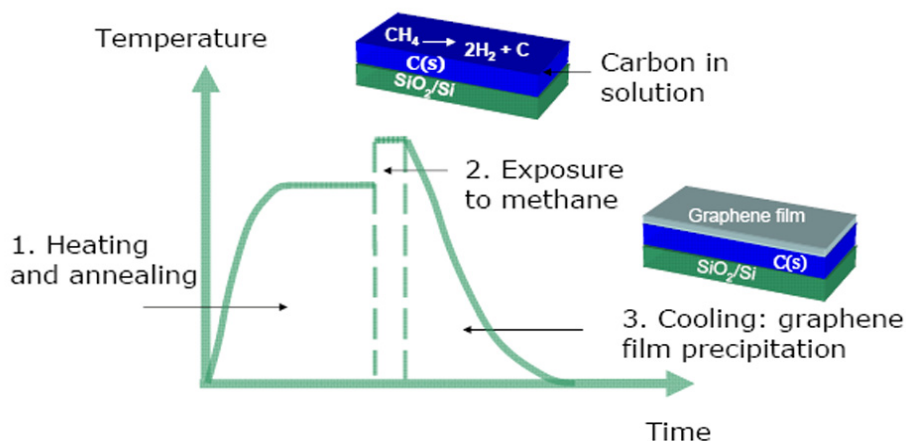
Figure 1. Illustration of the graphene growth process and its different stages (1-3). 1. The Ni film deposited on SiO_2/Si is heated to 900°C and annealed for 20 min under flowing H_2 and Ar (400 and 600 standard cubic centimeter per minute (sccm), respectively). Here, Ni grain growth and surface smoothening occurs. 2. Exposure to H_2 and CH_4 for 5 min. The flow rate of H_2 is always 1400 sccm in every run. The flow rates of CH_4 used in the results presented in Table 1 are 6, 7, 8, and 10 sccm corresponding to concentrations of 0.4 vol%, 0.5 vol%, 0.6 vol%, and 0.7 vol%, respectively. CH_4 is decomposed catalytically and the carbon produced is incorporated into the Ni film. 3. The substrate is cooled down from 1000 to 500°C under Ar, H_2 (700 sccm for both gases) and the same flow of CH_4 is used as in stage 2. Times for this step are 15 to 120 min corresponding to cooling rates between 33.0 and 4.2°C/min. At 500°C, the sample is taken out of the tube furnace and cooled rapidly to room temperature. For the case of a cooling rate of 100.0°C/min, the sample is simply taken out of the furnace and cooled down to room temperature.

Table 1. Types of graphene films obtained at different methane concentrations and cooling rates.

$X_{methane}$ (vol. %)	dT/dt (°C/min)						
	100.0	33.0	25.0	16.6	8.3	5.5	4.2
0.4	No graphene film						
0.5	No graphene film		B				
0.6	A		B				
0.7	A						

A = films of type A (Figs. 2(a) and 2(b)). B = films of type B (Figs. 2(c) and 2(d)).

During stage 2, CH_4 (typically around 0.5 vol%–1 vol% by controlling the flow rate) along with H_2 is allowed to flow over the Ni surface at 1000°C. CH_4 begins to decompose catalytically on the surface of Ni [21, 22] and carbon diffuses into the Ni film. After 5 min of CH_4 exposure, the Ni film is cooled down (stage 3) under Ar, H_2 and the same CH_4 concentration (see Fig. 1 and Table 1 for exact flow rates). Based on

previous models of non-equilibrium carbon segregation in Ni [19, 23], when the Ni–C solution is cooled down, graphene precipitates on the surface of the Ni film. We report that by controlling the amount of methane during our process and reducing the rate of substrate cooling in stage 3, it is possible to obtain graphene films consisting of mostly 1–2 LG (see Figure 2). The Ni films utilized are polycrystalline due to their deposition method (E-beam evaporation or sputtering) with a thickness of ~500 nm. The role of the Ni grain size on the thickness variation of the graphene films has been discussed previously [24]. In this work, Ni films were deposited under conditions which give two different average Ni grain sizes of a few microns or a few tens of microns after annealing (i.e., after stage 1). Results are compared using Ni substrates with both grain sizes. The use of these types of Ni films is attractive due to their relatively simple fabrication and low cost compared to single crystalline Ni. Transfer of the resulting graphene was done by wet-etching of the Ni film with a 3 wt% aqueous solution of hydrochloric acid. Before etching, a layer of poly(methyl methacrylate) (PMMA) was spincoated on the surface of the graphene film to serve as a support. The resulting PMMA/graphene layer was then manually laid on the target substrate (SiO$_2$/Si or TEM grids). The PMMA was finally removed by exposure to acetone in liquid or vapor form.
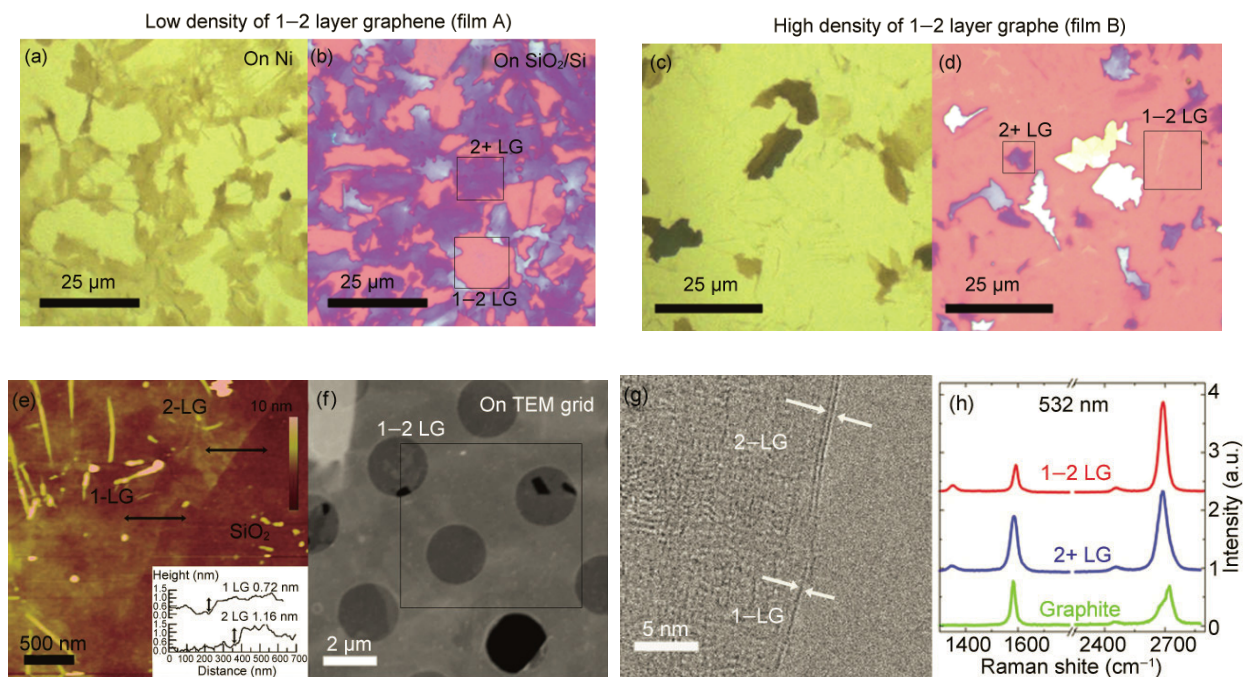
Figure 2. Two types of graphene films (types A and B) and their characterization. (a), (b) Type A film with low coverage of one- to two- layer regions (low $\theta_{1\text{-}2\,LG}$). (c), (d) Type B film with high coverage of one- to two- layer regions. (a) and (c) are optical images of the graphene films on Ni, (b) and (d) are optical images of the graphene films transferred to SiO$_2$/Si. Transfer to SiO$_2$/Si enables thickness analysis by optical contrast. (e) AFM image of a 1-2 layer region on SiO$_2$/Si of a type B film. Inset shows the cross sectional height of 1 and 2 LG measured along the lines shown in the AFM tepographical image. (f) SEM image of a 1-2 LG region of a type B film transferred to a TEM grid for thickness analysis. The regions remain freestanding across the circular openings of the grid. Dark areas suggest that the film broke at those sites. (g) TEM image of a region consisting of 1-2 LG in a type B film (pink background in (d)). (h) Representative Raman spectra collected from a type B film at regions consisting of 1-2 LG (shown in red) and 2+ LG (~5 L, shown in blue). The G´ peak at ~2700 cm^{-1} for 1-2 LG is a single Lorentzian peak. The Raman spectra of graphite pieces found in the film (yellow clusters in optical image (d)) are shown in green. The laser wavelength used was 514 nm with a laser power of 1 mW and acquisition time of 5 s.

Two types of graphene films (A and B, shown in Fig. 2) with contrasting thickness variations can be obtained by controlling the methane concentration during CVD ($X_{methane}$) and the rate of cooling (dT/dt). Table 1 shows the conditions under which each type of film can be grown. Films of type A consist mostly of multilayer graphene and are grown with high $X_{methane}$ (0.7 vol%). It is observed that the Ni grain size

plays a critical role in the thickness variation of the film, as also reported previously [24]. Multilayer graphene with more than two graphene layers (2+ LG) tends to segregate around the grain boundaries of the polycrystalline Ni fi lm [Figs. 2(a) and 2(b)]. The thinnest regions that were identified (1–2 LG) grow at the center of the large Ni grains of the catalytic Ni film. These observations suggest that Ni grain boundaries act as preferential nucleation sites for multilayer graphene or graphite. This can be explained by the fact that impurities in transition metals tend to segregate at grain boundaries [25, 26]. On closer scrutiny, comparison of Figs. 2(a) and 2(b) reveals that multilayer graphene was present at almost all the Ni grain boundaries, suggesting that the density of nucleation sites for graphene precipitation is high (as compared to graphene film type B which is discussed later). For a CH_4 concentration of 0.7 %—which always results in the growth of type A films—the sizes of 1–2 LG are independent of the cooling rate (see the summary in Table 2), but do depend strongly on the average grain size of the Ni film used for the synthesis. Therefore, Ni films with different average grain sizes produce 1–2 LG regions of different sizes [24].

Table 2. Description of films obtained with different CH_4 concentrations and cooling rates.

| $X_{methane}$ (vol. %)	Regime of dT/dt (°C/min)	
	High (100.0°C/min)	Low (<25°C/min)
0.5	No graphene film	B $\theta_{1\text{-}2\,LG}$ depends on cooling rate; ρ_{2+LG} is homogeneous across Ni surface; full coverage of the graphene film on the Ni surface
0.6	A $\theta_{1\text{-}2\,LG}$ similar to the size of Ni grains; ρ_{2+LG} is homogeneous across the graphene film; partial coverage of the graphene film on the Ni surface	B $\theta_{1\text{-}2\,LG}$ depends on cooling rate; ρ_{2+LG} is inhomogeneous across the graphene film; full coverage of the graphene film on the Ni surface
0.7	A $\theta_{1\text{-}2\,LG}$ similar to the size of Ni grains; ρ_{2+LG} is homogeneous across the graphene film; full coverage of the graphene film on the Ni surface	A $\theta_{1\text{-}2\,LG}$ similar to the size of Ni grains; ρ_{2+LG} is homogeneous across the graphene film; full coverage of the graphene film on the Ni surface

A = films of type A (Figs. 2(a) and 2(b)). B = films of type B (Figs. 2(c) and 2(d)) $\theta_{1\text{-}2}$ LG = area fraction occupied by one or two graphene layers. ρ_{2+LG} = number density of multilayer sites with more than two graphene layers.

Graphene films with their area consisting mostly of 1–2 LG (type B in Fig. 2) are grown by using intermediate $X_{methane}$ values (0.5%–0.6%) and low cooling rates (dT/dt < 25°C/min). For this case, the film thickness variation obtained is significantly different from that obtained with higher $X_{methane}$ (0.7%). It is observed that not all grain boundaries on the polycrystalline Ni show the nucleation of multilayers [Figs. 2(c) and 2(d)], resulting in an increase of the area fraction covered by 1–2 LG. AFM, TEM, Raman spectroscopy and optical microscopy were used to characterize these films [Figs. 2(e)–(h)]. The heights of 1- and 2-LG on SiO_2/Si as measured by AFM are 0.72 and 1.16 nm, respectively [Fig. 2(e)]. TEM confirmed that most of the film area consists of 1–2 LG [Figs. 2(f) and 2(g)]. The Raman G´ band (~2700 cm^{-1}) of 1- and 2-LG always has a single Lorentzian lineshape. For both cases, the linewidth usually lies in the range 30–40 cm^{-1}, suggesting the absence of interlayer coupling. Furthermore, the relative intensity of the G´ and G bands varies randomly between 1- and 2-LG regions, possibly due to differences in doping levels [27]. Also, no difference in G´ frequency is observed between the 1- and 2-LG regions probed [28]. Therefore, it is not possible to distinguish between 1- and 2-LG using Raman spectroscopy alone. This is better done by optical microscopy [see discussion below and Electronic Supplementary Material (ESM)] or direct observation in a TEM. Four point probe measurements of the sheet resistance of the films yield values of ~0.5 1 kΩ/sq and 3–5 kΩ/sq for films of types A and B, respectively. The difference in sheet resistance is attributed to the conduction through multilayer graphene which should have a larger contribution to the film conductivity in the case of films of type A.

The differences in the number of multilayer graphene sites between films of types A and B can be explained in terms of the differences in the methane concentrations and cooling rates used. Lower methane concentrations will result in relatively low carbon concentrations in the Ni film. Consequently,

this will promote a reduction of carbon segregation on the Ni surface during the cooling stage. The amount of segregation, for a given change in temperature dT/dt, depends on the magnitude of the solute oversaturation (which should be directly related to the methane flow rate) [29–31]. On the other hand, decreasing dT/dt may promote segregation under conditions closer to equilibrium, therefore reducing the density of multilayer sites [32]. Note that with 0.5% methane concentration, only films of type B were obtained, whereas if the methane concentration was increased to 0.7%, only films of type A were obtained. This is consistent with our ideas discussed above. Table 1 shows that at 0.6% methane, there was a transition from A to B type of film growth as the cooling rate was decreased. However, it was found that this methane concentration resulted in a partial graphene coverage of the Ni surface if high cooling rates (33–100°C/min) were used (see Table 2). For the same methane concentration, using low cooling rates (<25°C/min) resulted in full coverage but with an inhomogeneous density of multilayer sites. The best control over both graphene coverage and homogeneous density of multilayer sites was accomplished with methane concentrations of 0.5% and 0.7% for films of types A and B, respectively (see Table 2).

It was found that in type B films, grown with $X_{methane}$ = 0.5%, the area covered by 1–2 LG (θ_{1-2LG}) was dependent on the cooling rate (Table 2). Figure 3 shows that decreasing the cooling rate below 25°C/min during the segregation step further increased θ_{1-2LG} in type B films ($X_{methane}$ ~0.5%). In addition, the slower the cooling rate, the fewer the number of nucleation sites of multilayer graphene (ρ_{2+LG}). The decrease in the density of multilayer sites can be also attributed to a reduction of the segregation rate caused by the lowering of dT/dt. At low segregation rates, carbon atoms can diffuse for longer times before they coalesce to form graphene (diffusion limited nucleation) [30]. It can also be observed that as dT/dt decreased, not only did ρ_{2+LG} decrease but the thickness of the multilayer pieces increased. This can be seen by the increase in the number of yellow or white regions (graphite) and the reduction in the number of purple or blue regions on the graphene film [Figs. 3(a)–(c)]. This suggests that dT/dt may only have an effect on the density of multilayer sites, and not on the amount of carbon segregating. Consequently, in the case of our slowest cooling rates, if fewer nucleation sites are available for the same amount of carbon segregating at the surface, an increase in the thickness of the multilayer graphene regions must be expected.
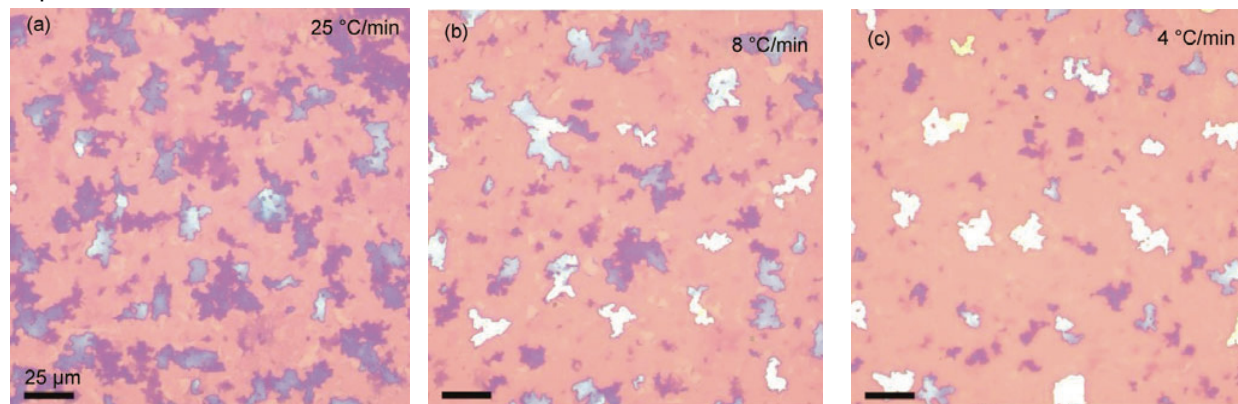
Figure 3. Effect of the cooling rate on type B films which were grown with a CH_4 concentration of 0.5%. (a)-(c) Optical images of graphene films transferred to SiO_2/Si grown with decreasing cooling rate as indicated. The number of nucleation sites with multilayer graphene decreases as the cooling rate decreases, leading to an increase of the 1-2 LG region (pink background). Scale bars are all 25 μm.

The cooling rate of the Ni film during graphene precipitation was used to obtain films with up to 87% of their area (θ_{1-2LG} = 0.87) composed of no more than two layers of graphene (of which the single layer area made up 5%–11% of the total film area). The area fraction θ_{1-2LG} increased as the cooling rate was decreased and it can be tuned from 0.60–0.87 for CVD processes using $X_{methane}$ ~0.5% (Figure 4). The density of sites consisting of multilayer graphene with more than two layers, ρ_{2+LG}, can be decreased by 50% on going from the highest to the lowest cooling rate tested (Fig. 4). The quantification of the area

percentage plotted in Fig. 4 was done by comparing optical images of the graphene films on SiO_2/Si with bare SiO_2/Si substrates. Each pixel of the optical images can be expressed in the RGB (red green blue) color model [33] which is used for image display and representation in electronic systems. In this model, the color of each pixel in an image is represented by the intensities of the three primary colors—red, green, and blue, hence used as its name. When graphene is present on 300 nm SiO_2/Si, it creates an enhanced absorption at wavelengths around 500 nm [34, 35] corresponding to the color green. Therefore, the green component, {G} of our optical images can be used to identify the contrast created by the CVD graphene film with respect to the underlying SiO_2 [Fig. 4(a)]. This enables us to identify regions with down to 1- and 2-LG in an automated way (see ESM). Such a contrast in {G} was also measured for pieces of exfoliated graphene [from highly oriented pyrolytic graphite (HOPG)] on SiO_2/Si and was used as a calibration for the identification of 1- or 2- LG derived from our CVD process (see ESM). The coverage, θ_{1-2LG}, plotted in Fig. 4(b) represents the fraction of pixels identified as containing no more than two graphene layers (pink background in images of Fig. 3). Optical images at 50× magnification, with 3900 by 3090 pixels (289 μm × 229 μm), were used for this analysis. It was also observed that θ_{1-2LG} is independent of the grain size of the Ni film used to synthesize graphene [Figs. 4(b) and 4(c)]. Two Ni grain sizes (L_1 and L_2) were used in our experiments and their images are shown in Figs. 4(d) and 4(e). Optical images of graphene grown on both Ni grain structures and transferred to SiO_2/Si are shown in Figs. 4(f)–(i). This comparison is important since the grain sizes of transition metal thin films vary depending on film thickness, residual stress and deposition conditions [36, 37]. Lastly, these films are also transferable to other substrate materials, similar to the way such transfers have been reported previously [15]. Graphene films of up to 1 in^2 in size and with high area fractions of 1–2 LG have been fabricated [Fig. 4(j)]. Their sizes are limited only by the size of the Ni film used and the CVD chamber size.
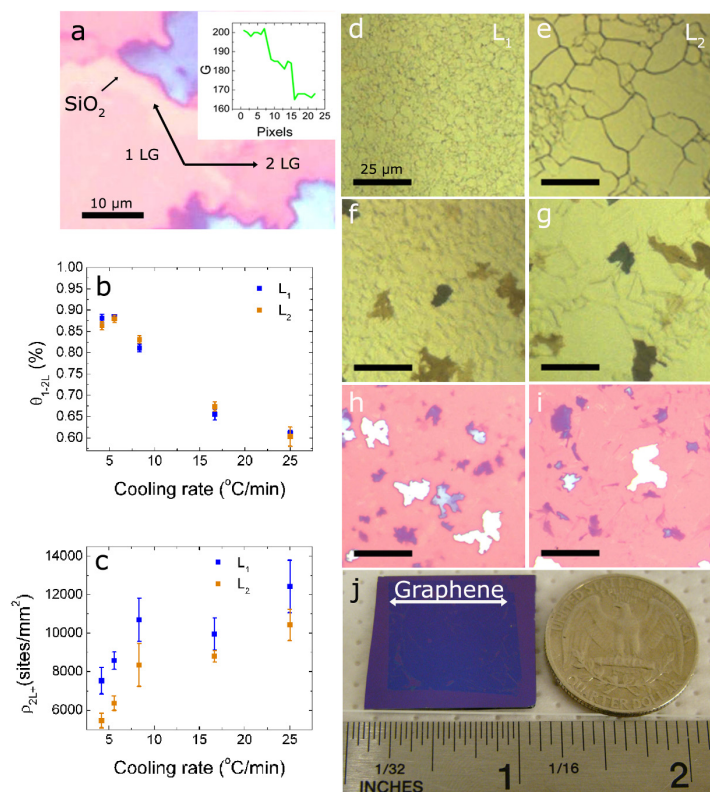
Figure 4. Quantification of single and bilayer graphene coverage of graphene films grown on Ni with different grain sizes (L_1 and L_2). (a) Optical recognition of 1- and 2-LG with the {G} values extracted from the RGB image of graphene films on SiO_2/Si. {G} decreases in a stepwise manner from bare SiO_2 to one and to two graphene layers (inset in (a)): {G}$_{bare\ SiO_2}$ =200 and the measured Δ{G} values for the 1-L and 2-L regions shown are 15 and 33, respectively (see inset). The expected Δ{G} for 1-L and 2-L HOPG are 16 and 30, respectively (see ESM). (b) Area fraction ($\theta_{1-2\ LG}$) covered by no more than two graphene layers as a function of cooling rate for graphene films synthesized with Ni grain sizes L_1 and L_2. (c) Number of sites per mm^2 with more than two graphene layers (ρ_{2+LG}) vs dT/dt. The two different Ni films with grain sizes L_1 and L_2 show a similar dependence on cooling rate. Optical images of the two grain sizes are shown in (d) and (e). Graphene films grown on the two types of Ni films before ((f) and (g)) and after transferring to SiO_2/Si ((h) and (i)). The area covered by 1-2 LG is independent of the Ni grain size. Scale bars in (d)-(i): 25 μm. (j) Photograph of a large graphene film with ~87% of its area covered by 1-2 LG. The size of the films fabricated is only limited by the sizes of the Ni film and the CVD chamber employed.

In conclusion, we have demonstrated the possibility of growing graphene films with up to 87% of their area composed of no more than two graphene layers and which can also be transferred to insulating substrates. This was accomplished by controlling both the carbon concentration and the substrate cooling rate during the CVD process. Under a suitable carbon concentration (0.5% CH_4 in our case), the cooling rate can be utilized to decrease the number of nucleation sites of multilayer graphene on the film (by a factor of two) and to increase significantly the area covered by sections with 1–2 LG. Further quantitative analysis (for example, the carbon concentration inside the Ni film for substrates treated with different CH_4 exposures and cooling rates) is currently being undertaken in order to gain a deeper understanding of this process. Nevertheless, our results suggest the possibility of dramatically improving the thickness uniformity of graphene films by controlling the process parameters in our method. Therefore, ambient pressure CVD may be a viable route to control the growth of single graphene layers over large scales.

Electronic Supplementary Material: Details of the automated recognition of regions of one- and twolayer graphene by computer programs using optical images are available in the online version of this article at http://dx.doi.org/10.1007/s12274-009-9059-y and are accessible free of charge.

References

[1]   K. S. Novoselov, D. Jiang, F. Schedin, T. J. Booth, V. V. Khotkevich, S. V. Morozov, and A. K. Geim, "Two-Dimensional Atomic Crystals," *Proceedings of the National Academy of Sciences of the United States of America* **102(30):** 10451-10453 (2005).

[2]   P. Blake, P. D. Brimicombe, R. R. Nair, T. J. Booth, D. Jiang, F. Schedin, L. A. Ponomarenko, S. V. Morozov, H. F. Gleeson, E. W. Hill, A. K. Geim, and K. S. Novoselov, "Graphene-Based Liquid Crystal Device," *Nano Letters* **8(6):** 1704-1708 (2008).

[3]   S. Stankovich, D. A. Dikin, R. D. Piner, K. A. Kohlhaas, A. Kleinhammes, Y. Jia, Y. Wu, S. T. Nguyen, and R. S. Ruoff, "Synthesis of Graphene-Based Nanosheets Via Chemical Reduction of Exfoliated Graphite Oxide," *Carbon* **45(7):** 1558-1565 (2007).

[4]   G. Eda, G. Fanchini, and M. Chhowalla, "Large-Area Ultrathin Films of Reduced Graphene Oxide as a Transparent and Flexible Electronic Material," *Nature Nanotechnology* **3(5):** 270-274 (2008).

[5]   Y. Hernandez, V. Nicolosi, M. Lotya, M. Blighe, Z. Sun, S. De, I. T. McGovern, B. Holland, M. Byrne, Y. K. Gun'ko, J. J. Boland, P. Niraj, G. Duesberg, S. Krishnamurthy, R. Goodhue, J. Hutchison, V. Scardaci, A. C. Ferrari, and J. N. Coleman, "High-Yield Production of Graphene by Liquid-Phase Exfoliation of Graphite," *Nature Nanotechnology* **3(9):** 563-568 (2008).

[6]   D. Li, M. B. Mueller, S. Gilje, R. B. Kaner, and G. G. Wallace, "Processable Aqueous Dispersions of Graphene Nanosheets," *Nature Nanotechnology* **3(2):** 101-105 (2008).

[7]   X. Li, G. Zhang, X. Bai, X. Sun, X. Wang, E. Wang, and H. Dai, "Highly Conducting Graphene Sheets and Langmuir-Blodgett Films," *Nature Nanotechnology* **3(9):** 538-542 (2008).

[8]   K. A. Worsley, P. Ramesh, S. K. Mandal, S. Niyogi, M. E. Itkis, and R. C. Haddon, "Soluble Graphene Derived From Graphite Fluoride," *Chemical Physics Letters* **445:** 51-56 (2007).

[9]   C. Berger, Z. M. Song, T. B. Li, X. B. Li, A. Y. Ogbazghi, R. Feng, Z. T. Dai, A. N. Marchenkov, E. H. Conrad, P. N. First, and W. A. de Heer, "Ultrathin Epitaxial Graphite: 2-D Electron Gas Properties and a Route Toward Graphene-Based Nanoelectronics," *Journal of Physical Chemistry B* **108(52):** 19912-19916 (2004).

[10] C. Berger, Z. M. Song, X. B. Li, X. S. Wu, N. Brown, C. Naud, D. Mayou, T. B. Li, J. Hass, A. N. Marchenkov, E. H. Conrad, P. N. First, and W. A. de Heer, "Electronic Confinement and Coherence in Patterned Epitaxial Graphene," *Science* **312(5777):** 1191-1196 (2006).

[11] P. W. Sutter, J-I. Flege, and E. A. Sutter, "Epitaxial Graphene on Ruthenium," *Nature Materials* **7(5):** 406-411 (2008).

[12] Y. Pan, D. X. Shi, and H. J. Gao, "Formation of Graphene on Ru(0001) Surface," *Chinese Physics* **16(11):** 3151-3153 (2007).

[13] A. Dato, V. Radmilovic, Z. H. Lee, J. Phillips, and M. Frenklach, "Substrate-Free Gas-Phase Synthesis of Graphene Sheets," *Nano Letters* **8(7):** 2012-2016 (2008).

[14] Q. K. Yu, J. Lian, S. Siriponglert, H. Li, Y. P. Chen, and S-S. Pei, "Graphene Segregated on Ni Surfaces and Transferred to Insulators," *Applied Physics Letters* **93(11):** 113103 1-3 (2008).

[15] A. Reina, X. T. Jia, J. Ho, D. Nezich, H. B. Son, V. Bulovic, M. S. Dresselhaus, and J. Kong, "Large Area, Few-Layer Graphene Films on Arbitrary Substrates by Chemical Vapor Deposition," *Nano Letters* **9(1):** 30-35 (2009).

[16] K. S. Kim, Y. Zhao, H. Jang, S. Y. Lee, J. M. Kim, K. S. Kim, J-H. Ahn, P. Kim, J-Y. Choi, and B. H. Hong, "Large-Scale Pattern Growth of Graphene Films for Stretchable Transparent Electrodes," *Nature* **457(7230):** 706-710 (2009).

[17] L. G. De Arco, Z. Yi, A. Kumar, and Z. Chongwu, "Synthesis, Transfer, and Devices of Single- and Few-Layer Graphene by Chemical Vapor Deposition," *IEEE Transactions on Nanotechnology* **8(2):** 135-138 (2009).

[18] D. Fujita and K. Yoshihara, "Surface Precipitation Process of Epitaxially Grown Graphite (0001) Layers on Carbon-Doped Nickel(111) Surface," *Journal of Vacuum Science and Technology A: Vacuum, Surfaces, and Films* **12(4):** 2134-2139 (1994).

[19] J. C. Shelton, H. R. Patil, and J. M. Blakely, "Equilibrium Segregation of Carbon to a Nickel (111) Surface: A Surface Phase Transition," *Surface Science* **43(2):** 493-520 (1974).

[20] E. Loginova, N. C. Bartelt, P. J. Feibelman, and K. F. McCarty, "Evidence for Graphene Growth by C Cluster Attachment," *New Journal of Physics* **10(9):** 093026 1-16 (2008).

[21] N. Z. Muradov, "How to Produce Hydrogen from Fossil Fuels Without CO_2 Emission," *International Journal of Hydrogen Energy* **18(3):** 211-215 (1993).

[22] S. Takenaka, Y. Shigeta, E. Tanabe, and K. Otsuka, "Methane Decomposition Into Hydrogen and Carbon Nanofibers Over Supported Pd-Ni Catalysts: Characterization of the Catalysts During the Reaction," *Journal of Physical Chemistry B* **108(23):** 7656-7664 (2004).

[23] D. Fujita and T. Homma, "Surface Precipitation of Graphite Layers on Carbon-Doped Nickel and Their Stabilization Effect Against Chemisorption and Initial Oxidation," *Surface and Interface Analysis* **19:** 430-434 (1992).

[24] S. Thiele, A. Reina, P. Healey, J. Kedzierski, P. Wyatt, P-L. Hsu, C. Keast, J. Schaefer, and J. Kong, "Engineering Polycrystalline Ni Films to Improve Thickness Uniformity of the Chemical-Vapor-Deposition-Grown Graphene Films," *Nanotechnology* **21(1):** 015601 1-8 (2010).

[25] Y. M. Wang, S. Cheng, Q. M. Wei, E. Ma, T. G. Nieh, and A. Hamza, "Effects of Annealing and Impurities on Tensile Properties of Electrodeposited Nanocrystalline Ni," *Scripta Materialia* **51(11):** 1023-1028 (2004).

[26] T. D. Shen, R. B. Schwarz, S. Feng, J. G. Swadener, J. Y. Huang, M. Tang, H. Z. Zhang, S. C. Vogel, and Y. S. Zhao, "Effect of Solute Segregation on the Strength of Nanocrystalline Alloys: Inverse Hall-Petch Relation," *Acta Materialia* **55(15):** 5007-5013 (2007).

[27] A. Das, S. Pisana, B. Chakraborty, S. Piscanec, S. K. Saha, U. V. Waghmare, K. S. Novoselov, H. R. Krishnamurthy, A. K. Geim, A. C. Ferrari, and A. K. Sood, "Monitoring Dopants by Raman Scattering in an Electrochemically Top-Gated Graphene Transistor," *Nature Nanotechnology* **3(4):** 210-215 (2008).

[28] D. S. Lee, C. Riedl, B. Krauss, K. von Klitzing, U. Starke, and J. H. Smet, "Raman Spectra of Epitaxial Fraphene on SiC and of Epitaxial Graphene Transferred to SiO_2," *Nano Letters* **8(12):** 4320-4325 (2008).

[29] J. R. Frade, "Kinetics of Nucleation and Growth, Part I: Reaction Controlled Growth," *Journal of Materials Science* **28(24):** 6715-6718 (1993).

[30] J. R. Frade, "Kinetics of Nucleation and Growth, Part II: Diffusion Controlled Growth," *Journal of Materials Science* **29(1):** 169-174 (1994).

[31] T. Gambaryan-Roisman, E. Litovsky, M. Shapiro, and A. Shavit, "Reaction-Diffusion Model of Surface and Grain Boundary Segregation Kinetics," *International Journal of Heat and Mass Transfer* **43(22):** 4135-4151 (2000).

[32] S. Song, Z. Yuan, and T. Xu, "Non-Equilibrium Segregation of Boron at Austenite Grain Boundaries," *Journal of Materials Science Letters* **10(20):** 1232-1234 (1991).

[33] J. D. Foley, A. van Dan, S. K. Feiner, and J. F. Hughes, *Computer Graphics: Principles and Practice* (New Jersey: Addison-Wesley Systems Programming Series, 1995).

[34] P. Blake, E. W. Hill, A. H. C. Neto, K. S. Novoselov, D. Jiang, R. Yang, T. J. Booth, and A. K. Geim, "Making Graphene Visible," *Applied Physics Letters* **91(6):** 063124 1-3 (2007).

[35]   S. Roddaro, P. Pingue, V. Piazza, V. Pellegrini, and F. Beltram, "The Optical Visibility of Graphene: Interference Colors of Ultrathin Graphite on SiO_2," *Nano Letters* **7(9):** 2707-2710 (2007).

[36]   C. V. Thompson, "Grain Growth in Thin Films," *Annual Review of Materials Science* **20:** 245-268 (1990).

[37]   C. V. Thompson and R. Carel, "Stress and Grain Growth in Thin Films," *Journal of the Mechanics and Physics of Solids* **44(5):** 657-673 (1996).

3.   Work Function Engineering of Graphene Electrode *via* Chemical Doping

Project Staff
Yumeng Shi, Ki Kang Kim, Alfonso Reina, Mario Hofmann, Lain-Jong Li, and Jing Kong

In this work, we demonstrate that graphene films synthesized by chemical vapor deposition (CVD) method can be used as thin transparent electrodes with tunable work function. By immersing the CVD-grown graphene films into $AuCl_3$ solution, Au particles were formed on the surface of graphene films by spontaneous reduction of metal ions. The surface potential of graphene films can be adjusted (by up to ~0.5 eV) by controlling the immersion time. Photovoltaic devices based on n-type silicon interfacing with graphene films were fabricated to demonstrate the benefit of an electrode with tunable work function. The maximum power conversion efficiency (PCE) achieved was ~0.08%, which is more than 40 times larger than the devices without chemical doping.

Indium tin oxide (ITO) has been widely used as electrodes in optoelectronic devices such as organic light-emitting diodes (OLEDs) and photovoltaic cells, due to its high transparency and good conductivity. The price of ITO has gone up significantly in recent years due to the limited indium resources. In addition, their chemical and electronic stability and mechanical flexibility limit their applications in flexible electronics [1]. With the emergence of novel flexible electronic devices, there is a growing demand for flexible electrodes, where conventional materials such as metal conductors and ITO may not reach the required bendability.

Two-dimensional networks of carbon nanotubes (CNTs) have been considered as a candidate to replace ITO because they possess excellent mechanical [2, 3] and electrical properties [4]. Recently, there has been tremendous research in the two-dimensional crystal graphene and its derived nanomaterials [5-8]. Graphene sheets can be considered as an unzipped CNT, which has unique physical properties such as high carrier mobility [5], long phase coherence length [9], fractional quantum Hall effect [10], bipolar supercurrent [11], suppression of the weak localization [12], deviation from the adiabatic Born-Oppenheimer approximation [13], etc. On the basis of these unique electronic properties and the two-dimensional planar structure, graphene also appears as a promising material for transparent electrodes [5, 14, 15]. Furthermore, besides good conductivity and transparency of the electrode, the performance and current density for semiconducting electronic devices, such as light-emitting diodes and field-effect transistors, strongly rely on the carrier injection efficiency through the contact between electrodes and semiconducting material layers [16, 17]. Therefore, the band alignment between electrodes and semiconductors and the surface property of the electrode have been an extensively investigated area [18-20]. Finding a certain conductive material with the desired work function for efficient carrier injection may sometimes be difficult. Both theoretical and experimental results have demonstrated that the Fermi energy shift of single-layer graphene (SLG) can be achieved through deliberate doping by aromatic molecules [21, 22], gas molecules [23], or electrostatic gating [5, 24]. These results suggest that controlling the work function of graphene electrodes is possible.

Tremendous progress has been achieved for the synthesis and characterization of graphene in the past few years [25]. Transparent graphene electrodes have been formed by either reducing graphene oxide [26] or a chemical bottom-up approach, where molecules of giant polycyclic aromatic hydrocarbons cross-link to form graphene nanosheets [27]. However, the conductivity of these films is still limited [28] and high enough electrical conductivity is required for good electrodes.
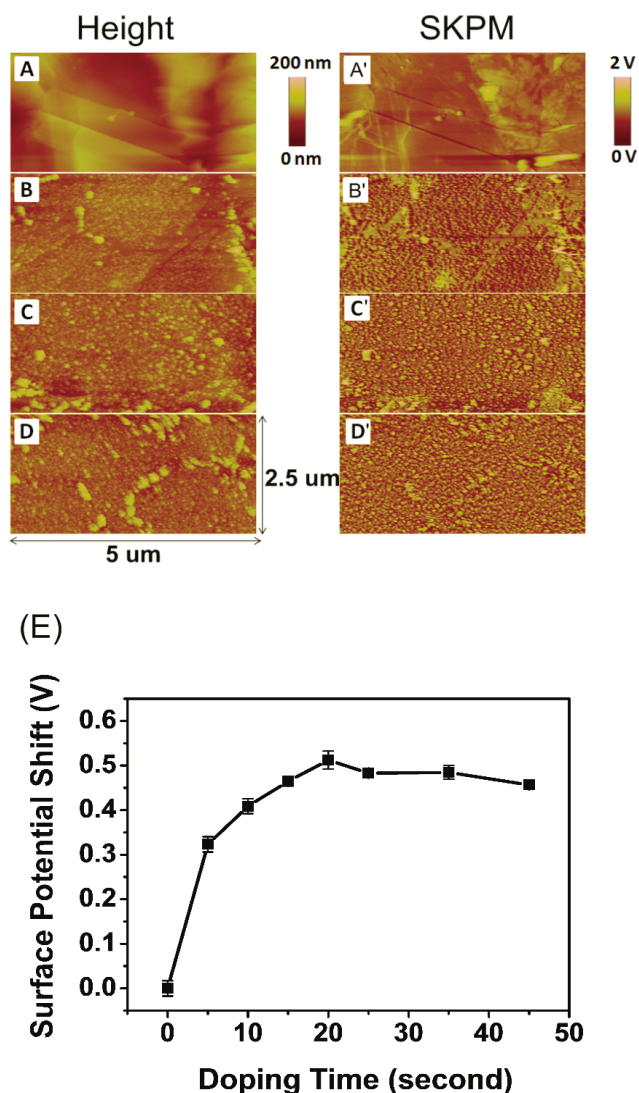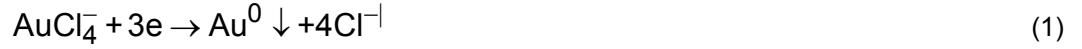

Figure 1. AFM images for as-grown CVD-G on 300 nm Ni (A) and those doped with AuCl$_3$ for (B) 5 s, (C) 25 s, and (D) 45 s. (A'-D'): Corresponding SKPM images. (E): Surface potential CVD-G on Ni substrate as a function of AuCl$_3$ doping time.

Recently, it has been demonstrated that continuous large-area graphene thin films can be synthesized by vacuum graphitization and ambient pressure chemical vapor deposition (APCVD) methods [29-34]. In this contribution, we use graphene films formed by chemical vapor deposition (CVD-G) as an ultrathin transparent electrode. We demonstrated that the work function of graphene can be tuned by AuCl$_3$ doping. AuCl$_3$ is a commonly used compound in doping organic conductors. The Au^{III} can be reduced to Au particles by the charge transfer from graphene which results in p-type doping behavior of graphene. AuCl$_3$ has been chosen for the stability of its doping effect. The surface potential change of graphene as a function of doping time was studied by measuring the contact potential difference (CPD) using Kelvin probe microscopy. Silicon photovoltaic devices with graphene electrodes were fabricated as a demonstration of the advantages of using CVD-G electrodes with tunable work function.

The images from the atomic force micrscopy (AFM) in Figure 1A-D and from scanning Kelvin probe microscopy (SKPM) in Figure 1A'-D' show the effect of AuCl$_3$ doping time on the surface morphology and surface potential of CVD-G, respectively. With longer doping time, it was observed that the size of Au particles became larger and the morphology changed. The formation of Au particles on CVD-G can be understood from an electrochemical perspective since the reduction potential of AuCl$_4^-$ ion (1.0 V) is higher than the reduction potential of graphene (0.22 V) [35]. In aqueous solutions, AuCl$_3$ forms a square planar complex, AuCl$_4^-$, and the following reaction takes place on graphene [36]:

$$AuCl_4^- + 3e \rightarrow Au^0 \downarrow + 4Cl^{-|} \tag{1}$$

We noticed that for samples with 20 s doping time, the Au particles uniformly cover the surface of the graphene film. For less than 20 s doping, Au particles tend to form on the wrinkles and thicker layers of CVDG [37]. As the doping time increases over 20 s, larger Au particles form and the size distribution of Au particles becomes broader. The SKPM images in Figure 1 indicate that the measured surface potential (V_{sur}) of Au particles is higher than adjacent graphene region (where color contrast is lower), and the V_{sur} difference between Au particles and graphene is from ~0.3 to ~0.8 V, depending on the Au particle size. The V_{sur} of Au particles is always more positive than that of adjacent graphene regions, suggesting that the doping caused by Au particles is p-type on graphene (i.e., Au particles receive electrons from graphene), which is consistent with the chemical reaction 1. This hole doping process results in the work function shift of the CVD-G. Figure 1E plots the V_{sur} shift (ΔV_{sur}) versus various AuCl$_3$ doping times. Since the CPD method relies on the stability of the work function of AFM tips and is also sensitive to the measurement environment, such as humidity and electric grounding, we took the V_{sur} as the averaged value over an area of 1 μm × 1 μm and the as-grown CVD-G film was used as a standard reference. Thus, ΔV_{sur} value are relative to the pristine as-grown sample:

$$\Delta V_{sur} = V_{sur} \text{ (sample after doping)} - V'_{sur} \text{ (as-grown graphene)} \tag{2}$$

For doping time less than 20 s, V_{sur} monotonically increases with doping time to about 0.5 V, and as the doping time further increases, the V_{sur} reduces slightly. Thus SKPM data indicate that the work function of CVD-G can be tuned by chemical doping and exposing to AuCl$_3$ results in electrons being withdrawn from CVD-G by the formation of Au particles, which give rise to an up-shift of V_{sur}. The surface potential measurements were consistent with electric transport measurements of CVD-G field-effect transistors in our previous experiments [38]. The slight down-shift for longer doping time is unclear at this stage and will be subject to further investigation. One mechanism could be the hygroscopic nature of AuCl$_3$ at higher concentrations. The water molecule could affect the charge transfer behavior between graphene and AuCl$_3$.

The benefit for having a transparent electrode with tunable work function will be demonstrated subsequently by enhancing the performance of a photovoltaic device. After CVD synthesis, the graphene films were transferred to n-Si substrates by coating a thin layer of PMMA on top of graphene film. The underlying Ni film was etched by Ni enchant (TFB commercial etchant from Transene). Then the graphene/PMMA film was transferred to AuCl$_3$ solution for chemical doping. After AuCl$_3$ doping, the sheet resistance of graphene film decreases from 400 to ~100 Ω/sq (see [37] for details). The device fabrication procedure is schematically shown in Figure 2. Using CVD synthesis and the PMMA transfer method, the size of graphene conducting film can be easily scaled up without a fundamental limit.

Using the PMMA transferred CVD-G film, we fabricated photovoltaic diodes with a structure as shown in Figure 2. In order to demonstrate the effect of the work function shift on the device performance, the current density of several diodes under varying biases is compared in Figure 3A. These devices were measured with and without AM 1.5 illuminations for pristine CVD-G electrode and the CVD-G film with 20 s AuCl$_3$ doping. The devices show clear photovoltaic behaviors, which are similar to the previous reported work of carbon nanotube film/n-Si p–n junction solar cells [39, 40]. Without illumination, both devices show a typical diode behavior, but the open circuit voltage (V_{oc}) and short circuit current (I_{sc}) are dramatically improved for the device with 20 s AuCl$_3$ doped CVD-G. More detailed AM 1.5 measurements for the devices with various doping time are shown in Figure 3B. The device containing the 20 s AuCl$_3$ doped CVD-G film displays the highest V_{oc} and I_{sc}. For longer doping times, both of the V_{oc} and I_{sc} drop and it can be noticed that for the sample with extremely long doping times, for example, 20 min, the electrical behavior shows no large difference to 30 s doping, which is consistent with the SKPM results. The device performance as a function of AuCl$_3$ doping time is plotted in Figure 3C. The

device with 20 s AuCl$_3$ doping shows the best photovoltaic performance. This observation can be explained by the SKPM reults in Figure 1E. Figure 3D schematically demonstrated the effect of work function change of graphene electrodes on the device performance. The work function of graphene is as large as graphite, ~4.66 eV [24, 41-43], and our SKPM measurement shows that with AuCl$_3$ modification the work function of graphene film can be up-shifted within the range of 0.5 eV.
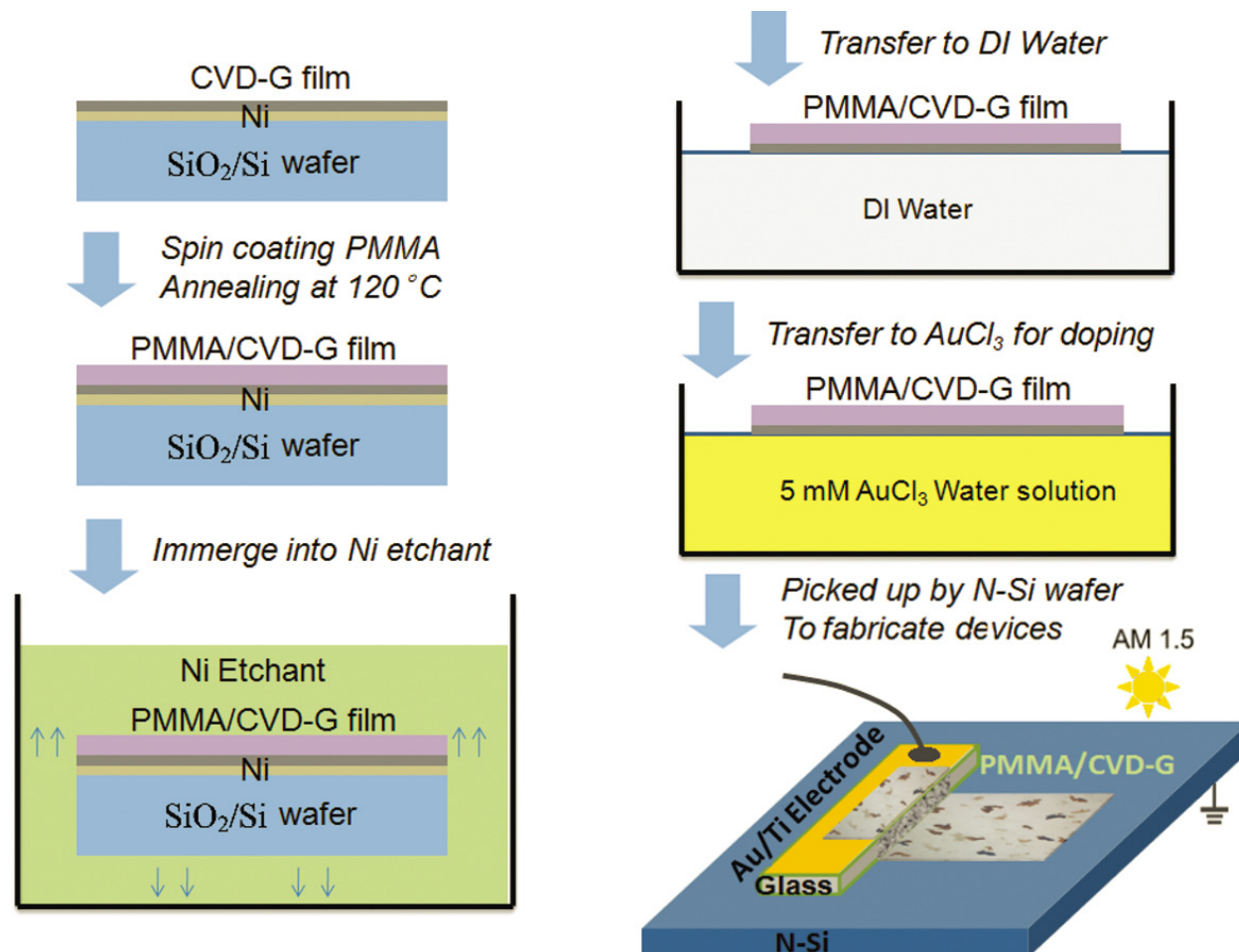
Figure 2. Schematic diagram of the transferring and device fabrication process. The graphene films are synthesized by an APCVD method on a SiO$_2$/Si wafer (300 nm thermal oxide) with 300 nm Ni film deposited in advance. The PMMA/CVD-G film was finally transferred to an n-type Si substrate for device fabrication.

It has been reported that a heterojunction can be formed between carbonaceous (or graphitic) thin films and n-type silicon [44, 45]. Under photoillumination, electron and hole pairs are generated in n-Si, similar to the case of carbon nanotube/n-Si solar cell [46]; the photogenerated electrons are directed toward the n-Si, while holes are injected into the graphene electrodes, due to the built-in electric field at the Si/graphene junction. However, unlike p-type semiconducting carbon nanotube, here graphene is a zero band gap material and it is simply treated as a metal. Therefore, the open circuit voltage corresponds to the amount of forward bias on the solar cell due to the bias of the solar cell junction with the light-generated current. Similar to the case for metal-on Si Schottky barrier solar cell [47], V_{oc} can be expressed as [48, 49]

$$V_{OC} = n\left[q\Phi_B + (kT/q)\ln\left(I_s/A_e A^* T^2\right) \right]$$

(3)
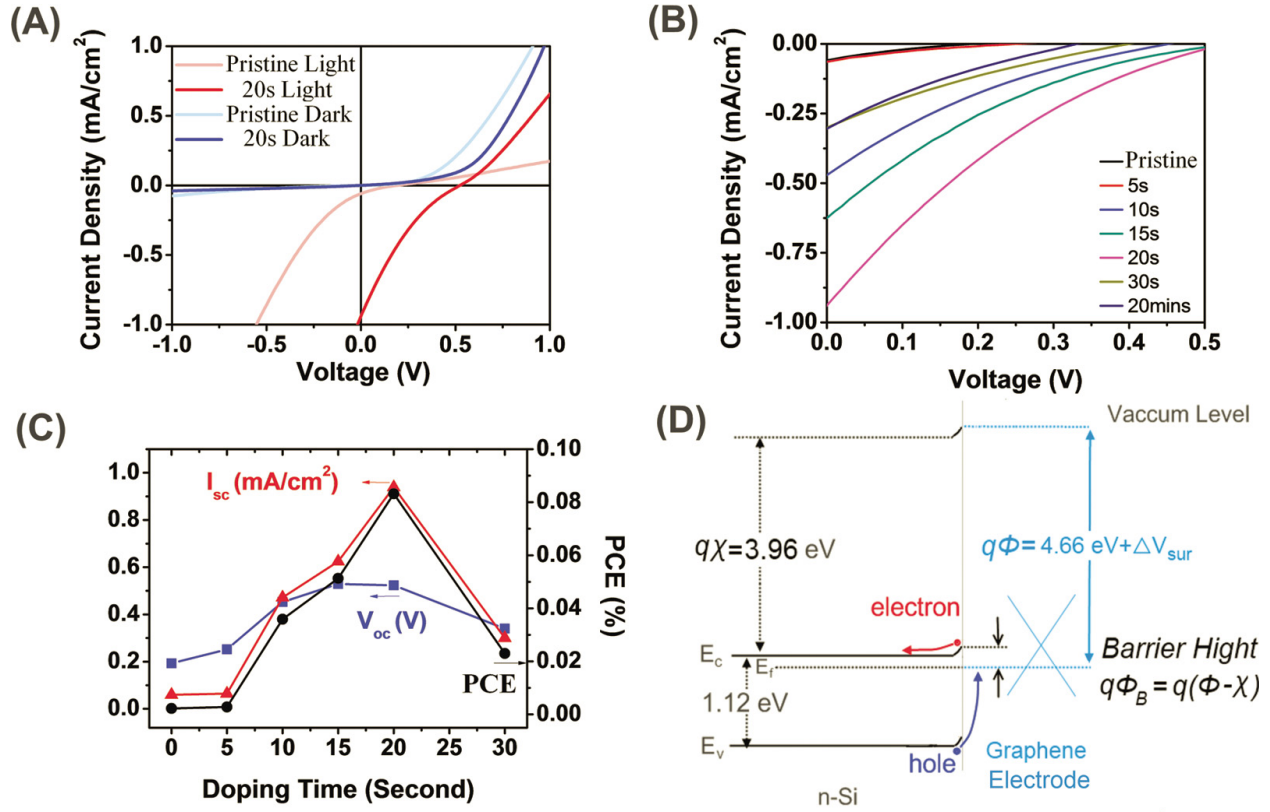
Figure 3. (A) Typical electrical measurement of pristine and 20 s AuCl$_3$ doped CVD-G/n-Si photovoltaic devices. (B) Current-voltage plots of the devices with different doping time from 5 s to 20 min under AM1.5 illumination. (C) Comparison of I_{sc}, V_{oc}, and PCE for different doping time. (D) Schematic illustration of the photovoltaic devices' band energy diagram (values obtained from [40]).

where n is the diode ideality factor, Φ_B is the barrier height, T is the working temperature, I_s is the diode saturation current, A_e and A^* are the contact area of the diode and the Richardson constant, respectively. Thus, the surface potential modification (or work function engineering) of graphene electrodes results in different barrier heights between Si and graphene, which provides tunability for the V_{oc} in the proposed n-Si/graphene photovoltaic devices. Besides the work function engineering effect, doping with Au particles affects the output characteristics of the photovoltaic device in several other ways. First, the doping also affects the carrier concentration of the graphene film, which further changes the sheet resistance of the graphene film [37]. A reduction in sheet resistance could also contribute to the change of short circuit current. Figure 3C clearly shows the evolution of V_{oc}, I_{sc} and power conversion efficiency (PCE) consistent with the V_{sur} shift in Figure 1E. Also, with a short AuCl$_3$ doping time, the Au particle layer is very thin, and the interface dipole between graphene and Au particles is expected to contribute strongly to the charge-injection process. With the increase of doping time, other effects such as transparency of the graphene film and the morphology-induced sheet resistance change need to be taken into consideration for device integration. A highest PCE achieved is ~0.08%, which is 40 times larger than the device without chemical doping. This value is comparable with the reported multiwalled CNT/n-Si solar cell devices [40]. It is suggested that the PCE of devices could be further improved by inserting a suitable p-type material between n-type Si and CVD-G electrodes or by opening the band gap of graphene. In summary, the chemical doping with Au particles can control the surface properties of graphene films, and the surface potential shift is able to explain the electrical characteristics for the diodes.

In conclusion, our EFM results show that the chemical doping of CVD-G with $AuCl_3$ causes a surface potential up-shift up to 0.5 eV, which is attributed to the hole doping process from Au particles. When n-type Si is covered by the CVD-G films, photoinduced charge seperation can be observed. The CVD-G electrodes offer more flexibility in improving electric properties of the photovoltaic devices due to work function engineering. Our results suggest a new strategy for charge harvesting by graphene films. The detailed photoelectrical behaviors of CVD-G/semiconducting composite devices, particularly the graphene electrode contacts are worthy of further investigation. The capability of tailoring electrical properties of graphene is potentially useful for optoelectronics.

Experimental Section. Few-layer graphene (FLG) film was synthesized by CVD method using 300 nm Ni-coated Si/SiO_2 substrates. The Ni substrates were annealed in the CVD chamber with H_2 and Ar (H_2/Ar = 400:600 sccm) for 20 min at 1000°C. CH_4 (4 sccm) along with H_2 (1400 sccm) was then flowed at 1000°C for 5 min to carburize the Ni film. Finally, the Ni film was cooled to 500°C with a cooling rate of 5°C/min under CH_4/H_2/Ar = 4:700:700 sccm, in order to control the thickness of graphene films. For the as-grown FLG films, one or two graphene layers were formed in most areas (see Supporting Information Figure S1). Details on the graphene film growth were reported elsewhere [32, 33]. Atomic force microscopy (AFM), Raman spectroscopy, and transmission electron microscopy (TEM) techniques were used to characterize the CVD-synthsized FLG as described in [32] and [33]. After CVD-G growth, the sample was immersed into $AuCl_3$ aqueous solution with a concentration of 5 mM for various durations. Then the sample was rinsed with DI water and blow-dried by nitrogen gas. In order to have a better grounding, the bottom Ni layer was not removed for the sample used for SKPM measurement.
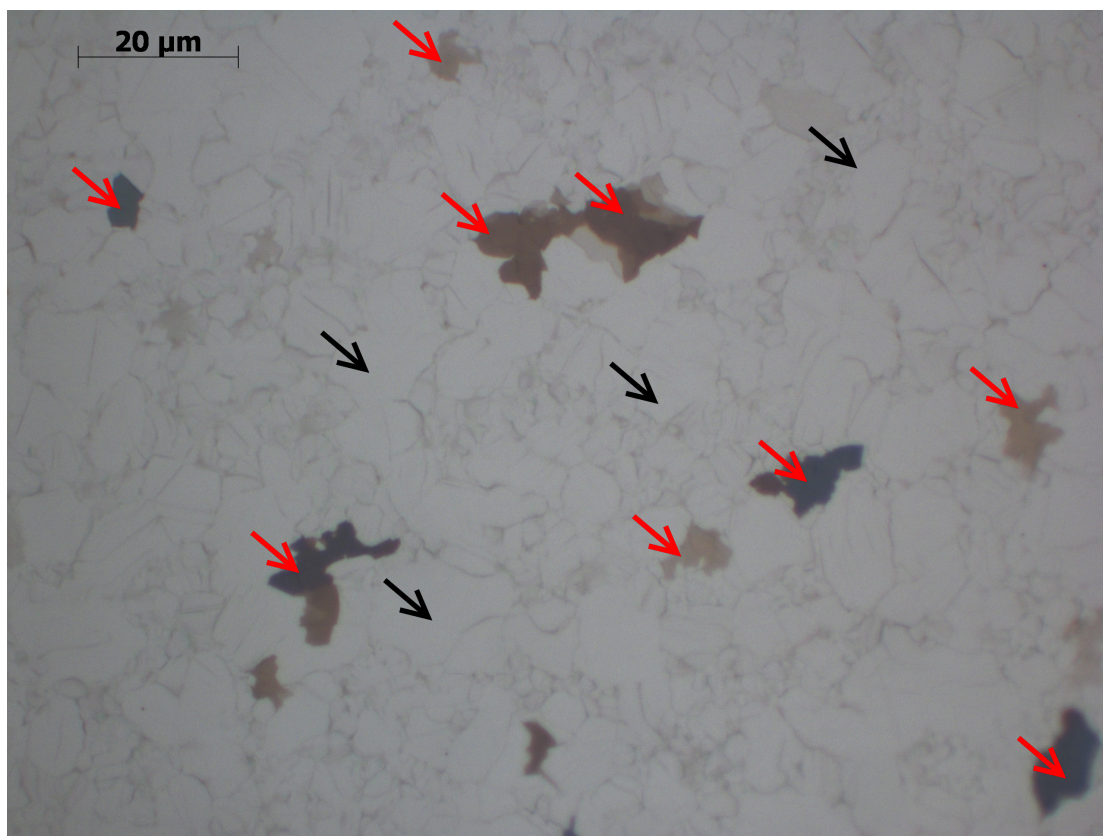
The surface potential (V_{sur}) of CVD-G before and after doping with $AuCl_3$ was measured by a dual-pass technique in tapping mode using the scanning Kelvin probe method (SKPM) based on an AFM system

Dimension 3000 from Veeco Metrology Group with NanoScope Signal Access Module. The measurement was conducted in air with Olympus (OMCL-AC240TM) Pt-coated cantilevers. The tip curvature radius is ~15 nm, quality factor ~190, spring constant 2 N/m, resonance frequency ~70 kHz, and cantilever length 240 μm. The CPD value between tip and sample surface was taken as the averaged value over an area of 1 μm × 1 μm. The standard deviation of the experiment was 10 mV.

The surface potential study was performed by a dual-pass technique in tapping mode. Topography information (AFM image) was acquired in the first scan; the second scan was then performed while the tip was maintained at a constant distance (10 nm above the sample surface). Both a DC signal and an AC signal at the resonant frequency of the cantilever are applied to the metal-coated AFM probe while the tip is lifted up. If a potential difference (ΔV_{sur}) exists between the tip and the sample surface, the signal creates a varying electrostatic force, causing an oscillating motion in the cantilever. The ΔV_{sur} is measured by adjusting the DC voltage until there is no DC potential difference. The DC voltage is recorded as the CPD value.

Photovoltaic devices were fabricated based on n-Si substrate with a resistivity around 5 Ω · cm. The as-grown CVD-G film was coated with a thin layer of PMMA (~100 nm) by spin coating to avoid the breaking of graphene film [50]. After etching the underlying polycrystalline Ni with Ni etchant, the PMMA/CVD-G film was transferred to DI water or additionally 5 mM $AuCl_3$ aqueous solution for chemical doping. After that, the film was transferred back to water and suspended on the surface of DI water. The film was later picked up by an n-type silicon substrate with an attached insulating glass cover slide. Ti (10 nm) and Au (200 nm) were evaporated on the top side of the glass slide in advance, which forms the upper electrode connects to the PMMA/CVD-G film. The rest of the PMMA/CVD-G film was brought in firm contact with the Si surface after careful blow drying with N_2 gas. The bottom electrodes were formed by connecting electrical wires to the back side of Si using silver paint. The area of the PMMA/CVD-G film on top of Si is 3 mm × 3 mm. The photovoltaic devices were irradiated under a solar simulator at AM 1.5 with a light intensity of 100 mW. Electrical testing was performed by an Agilent 4156C precision semiconductor parameter analyzer.

References

[1] Z. Chen, B. Cotterell, W. Wang, E. Guenther, and S.-J. Chua, "A Mechanical Assessment of Flexible Optoelectronic Devices," *Thin Solid Films* **394(1-2):** 201-205 (2001).
[2] J. P. Lu, "Elastic Properties of Carbon Nanotubes and Nanoropes," *Physical Review Letters* **79(7):** 1297-1300 (1997).
[3] V. N. Popov, V. E. Van Doren, and M. Balkanski, "Elastic Properties of Single-Walled Carbon Nanotubes," *Physical Review B* **61(4):** 3078-3084 (2000).
[4] T. W. Ebbesen, H. J. Lezec, H. Hiura, J. W. Bennett, H. F. Ghaemi, and T. Thio, "Electrical Conductivity of Individual Carbon Nanotubes," *Nature* **382(6586):** 54-56 (1996).
[5] K. S. Novoselov, A. K. Geim, S. V. Morozov, D. Jiang, Y. Zhang, S. V. Dubonos, I. V. Grigorieva, and A. A. Firsov, "Electric Field Effect in Atomically Thin Carbon Films," *Science* **306(5696):** 666-669 (2004).
[6] A. K. Geim and K. S. Novoselov, "The Rise of Graphene," *Nature Materials* **6(3):** 183-191 (2007).
[7] A. K. Geim, "Graphene: Status and Prospects," *Science* **324(5934):** 1530-1534 (2009).
[8] C. N. R. Rao, A. K. Sood, R. Voggu, and K. S. Subrahmanyam, "Some Novel Attributes of Graphene," *Journal of Physical Chemistry Letters* **1(2):** 572-580 (2010).
[9] F. Miao, S. Wijeratne, Y. Zhang, U. C. Coskun, W. Bao, and C. N. Lau, "Phase-Coherent Transport in Graphene Quantum Billiards," *Science* **317(5844):** 1530-1533 (2007).
[10] Y. Zhang, Y.-W. Tan, H. L. Stormer, and P. Kim, "Experimental Observation of the Quantum Hall Effect and Berry's Phase in Graphene," *Nature* **438(7065):** 201-204 (2005).
[11] H. B. Heersche, P. Jarillo-Herrero, J. B. Oostinga, L. M. K. Vandersypen, and A. F. Morpurgo, "Bipolar Supercurrent in Graphene," *Nature* **446(7131):** 56-59 (2007).

[12]   S. V. Morozov, K. S. Novoselov, M. I. Katsnelson, F. Schedin, L. A. Ponomarenko, D. Jiang, and A. K. Geim, "Strong Suppression of Weak Localization in Graphene," *Physical Review Letters* **97(1):** 016801 1-4 (2006).

[13]   S. Pisana, M. Lazzeri, C. Casiraghi, K. S. Novoselov, A. K. Geim, A. C. Ferrari, and F. Mauri, "Breakdown of the Adiabatic Born-Oppenheimer Approximation in Graphene," *Nature Materials* **6(3):** 198-201 (2007).

[14]   S. Watcharotone, D. A. Dikin, S. Stankovich, R. Piner, I. Jung, G. H. B. Dommett, G. Evmenenko, S.-E. Wu, S.-F. Chen, C.-P. Liu, S. T. Nguyen, and R. S. Ruoff, "Graphene-Silica Composite Thin Films as Transparent Conductors," *Nano Letters* **7(7):** 1888-1892 (2007).

[15]   C. Gomez-Navarro, R. T. Weitz, A. M. Bittner, M. Scolari, A. Mews, M. Burghard, and K. Kern, "Electronic Transport Properties of Individual Chemically Reduced Graphene Oxide Sheets," *Nano Letters* **7(11):** 3499-3503 (2007).

[16]   P. A. Cox, *The Electronic Structure and Chemistry of Solids* (New York: Oxford University Press, 1987), p. xi and p. 259.

[17]   Y. Shi, S.-C. Luo, W. Fang, K. Zhang, E. M. Ali, F. Y. C. Boey, J. Y. Ying, J. Wang, H.-H. Yu, and L.-J. Li, "Work Function Engineering of Electrodes Via Electropolymerization of Ethylene-dioxythiophenes and Its Derivatives," *Organic Electronics* **9(5):** 859-863 (2008).

[18]   X. Crispin, V. Geskin, A. Crispin, J. Cornil, R. Lazzaroni, W. R. Salaneck, and J.-L. Bredas, "Characterization of the Interface Dipole at Organic/Metal Interfaces," *Journal of the American Chemical Society* **124(27):** 8131-8141 (2002).

[19]   X. Cui, M. Freitag, R. Martel, L. Brus, and P. Avouris, "Controlling Energy-Level Alignments at Carbon Nanotube/Au Contacts," *Nano Letters* **3(6):** 783-787 (2003).

[20]   P. Zabel, T. Dittrich, Y.-L. Liao, C.-Y. Lin, K.-T. Wong, F. Fungo, L. Fernandez, and L. Otero, "Engineering of Gold Surface Work Function by Electrodeposition of Spirobifluorene Donor-Acceptor Bipolar Systems," *Organic Electronics* **10(7):** 1307-1313 (2009).

[21]   B. Das, R. Voggu, C. S. Rout, and C. N. R. Rao, "Changes in the Electronic Structure and Properties of Graphene Induced by Molecular Charge-Transfer," *Chemical Communications* **41(7):** 5155-5157 (2008).

[22]   X. Dong, D. Fu, W. Fang, Y. Shi, P. Chen, and L.-J. Li, "Doping Single-Layer Graphene With Aromatic Molecules," *Small* **5(12):** 1422-1426 (2009).

[23]   F. Schedin, A. K. Geim, S. V. Morozov, E. W. Hill, P. Blake, M. I. Katsnelson, and K. S. Novoselov, "Detection of Individual Gas Molecules Adsorbed on Graphene," *Nature Materials* **6(9):** 652-655 (2007).

[24]   Y.-J. Yu, Y. Zhao, S. Ryu, L. E. Brus, K. S. Kim, and P. Kim, "Tuning the Graphene Work Function by Electric Field Effect," *Nano Letters* **9(10):** 3430-3434 (2009).

[25]   C. N. R. Rao, A. K. Sood, K. S. Subrahmanyam, and A. Govindaraj, "Graphene: The New Two-Dimensional Nanomaterial," *Angewandte Chemie, International Edition* **48(42):** 7752-7777 (2009).

[26]   Z. Liu, Q. Liu, Y. Huang, Y. Ma, S. Yin, X. Zhang, W. Sun, and Y. Chen, "Organic Photovoltaic Devices Based on a Novel Acceptor Material: Graphene," *Advanced Materials* **20(20):** 3924-3930 (2008).

[27]   X. Wang, L. Zhi, N. Tsao, Z. Tomovic, J. Li, and K. Mullen, "Transparent Carbon Films as Electrodes in Organic Solar Cells," *Angewandte Chemie, International Edition* **47(16):** 2990-2992 (2008).

[28]   C.-Y. Su, Y. Xu, W. Zhang, J. Zhao, X. Tang, C.-H. Tsai, and L.-J. Li, "Electrical and Spectroscopic Characterizations of Ultra-Large Reduced Graphene Oxide Monolayers," *Chemistry of Materials* **21(23):** 5674-5680 (2009).

[29]   K. S. Kim, Y. Zhao, H. Jang, S. Y. Lee, J. M. Kim, K. S. Kim, J.-H. Ahn, P. Kim, J.-Y. Choi, and B. H. Hong, "Large-Scale Pattern Growth of Graphene Films for Stretchable Transparent Electrodes," *Nature* **457(7230):** 706-710 (2009).

[30]   C. Berger, Z. Song, X. Li, X. Wu, N. Brown, C. Naud, D. Mayou, T. Li, J. Hass, A. N. Marchenkov, E. H. Conrad, P. N. First, and W. A. de Heer, "Electronic Confinement and Coherence in Patterned Epitaxial Graphene," *Science* **312(5777):** 1191-1196 (2006).

[31] P. W. Sutter, J.-I. Flege, and E. A. Sutter, "Epitaxial Graphene on Ruthenium," *Nature Materials* **7(5):** 406-411 (2008).

[32] A. Reina, X. T. Jia, J. Ho, D. Nezich, H. B. Son, V. Bulovic, M. S. Dresselhaus, and J. Kong, "Large Area, Few-Layer Graphene Films on Arbitrary Substrates by Chemical Vapor Deposition," *Nano Letters* **9(1):** 30-35 (2009).

[33] A. Reina, S. Thiele, X. Jia, S. Bhaviripudi, M. S. Dresselhaus, J. A. Schaefer, and J. Kong, "Growth of Large-Area Single- and Bi-Layer Graphene by Controlled Carbon Precipitation on Polycrystalline Ni Surfaces," *Nano Research* **2(6):** 509-516 (2009).

[34] X. Li, W. Cai, J. An, S. Kim, J. Nah, D. Yang, R. Piner, A. Velamakanni, I. Jung, E. Tutuc, S. K. Banerjee, L. Colombo, and R. S. Ruoff, "Large-Area Synthesis of High-Quality and Uniform Graphene Films on Copper Foils," *Science* **324(5932):** 1312-1314 (2009).

[35] B. Shan and K. Cho, "First Principles Study of Work Functions of Single Wall Carbon Nanotubes," *Physical Review Letters* **94(23):** 236602 1-4 (2005).

[36] H. C. Choi, M. Shim, S. Bangsaruntip, and H. Dai, "Spontaneous Reduction of Metal Ions on the Sidewalls of Carbon Nanotubes," *Journal of the American Chemical Society* **124(31):** 9058-9059 (2002).

[37] K. K. Kim, A. Reina, Y. Shi, H. Park, L.-J. Li, Y. H. Lee, and J. Kong, "Enhancing the Conductivity of Transparent Graphene Films Via Doping," Nanotechnology **21(28):** 285205 1-6 (2010).

[38] X. Dong, Y. Shi, W. Huang, P. Chen, and L.-J. Li, "Electrical Detection of DNA Hybridization With Single-Base Specificity Using Transistors Based on CVD-Grown Graphene Sheets," *Advanced Materials* **22(14):** 1649-1653 (2010).

[39] J. Wei, Y. Jia, Q. Shu, Z. Gu, K. Wang, D. Zhuang, G. Zhang, Z. Wang, J. Luo, A. Cao, and D. Wu, "Double-Walled Carbon Nanotube Solar Cells," *Nano Letters* **7(8):** 2317-2321 (2007).

[40] Y. Jia, J. Wei, K. Wang, A. Cao, Q. Shu, X. Gui, Y. Zhu, D. Zhuang, G. Zhang, B. Ma, L. Wang, W. Liu, Z. Wang, J. Luo, and D. Wu, "Nanotube-Silicon Heterojunction Solar Cells," *Advanced Materials* **20(23):** 4594-4598 (2008).

[41] T. Filleter, K. V. Emtsev, T. Seyller, and R. Bennewitz, "Local Work Function Measurements of Epitaxial Graphene," *Applied Physics Letters* **93(13):** 133117 1-3 (2008).

[42] T. Takahashi, H. Tokailin, and T. Sagawa, "Angle-Resolved Ultraviolet Photoelectron Spectroscopy of the Unoccupied Band Structure of Graphite," *Physical Review B* **32(12):** 8317-8324 (1985).

[43] S. S. Datta, D. R. Strachan, E. J. Mele, and A. T. C. Johnson, "Surface Potentials and Layer Charge Distributions in Few-Layer Graphene Films," *Nano Letters* **9(1):** 7-11 (2009).

[44] K. M. Krishna, Y. Nukaya, T. Soga, T. Jimbo, and M. Umeno, "Solar Cells Based on Carbon Thin Films," *Solar Energy Materials and Solar Cells* **65(1):** 163-170 (2001).

[45] S. Tongay, T. Schumann, and A. F. Hebard, "Graphite Based Schottky Diodes Formed on Si, GaAs, and 4H-SiC Substrates," *Applied Physics Letters* **95(22):** 222103 1-3 (2009).

[46] Z. Li, V. P. Kunets, V. Saini, Y. Xu, E. Dervishi, G. J. Salamo, A. R. Biris, and A. S. Biris, "Light-Harvesting Using High Density *p*-Type Single Wall Carbon Nanotube/*n*-Type Silicon Heterojunctions," *ACS Nano* **3(6):** 1407-1414 (2009).

[47] W. A. Anderson and R. A. Milano, "I-V Characteristics for Silicon Schottky Solar Cells," *Proceedings of the IEEE* **63(1):** 206-208 (1975).

[48] J. P. Ponpon and P. Siffert, "Open-Circuit Voltage of MIS Silicon Solar Cells," *Journal of Applied Physics* **47(7):** 3248-3251 (1976).

[49] T. C. Lee, T. P. Chen, H. L. Au, S. Fung, and C. D. Beling, "The Effect of the Temperature Dependence of the Ideality Factor on Metal-Semiconductor Solar Devices," *Semiconductor Science and Technology* **8(7):** 1357-1360 (1993).

[50] A. Reina, H. Son, L. Jiao, B. Fan, M. S. Dresselhaus, Z. Liu, and J. Kong, "Transferring and Identification of Single- and Few-Layer Graphene on Arbitrary Substrates," *Journal of Physical Chemistry C* **112(46):** 17741-17744 (2008).

Publications

Journal Articles

Y. Shi, K. K. Kim, A. Reina, M. Hofmann, L-J. Li, and J. Kong, "Work Function Engineering of Graphene Electrode Via Chemical Doping," *ACS (American Chemical Society) Nano* **4(5):** 2689-2694 (May 2010).

B. G. Choi, H. Park, T. J. Park, M. H. Yang, J. S. Kim, S-Y. Jang, N. S. Heo, S. Y. Lee, J. Kong, and W. H. Hong, "Solution Chemistry of Self-Assembled Graphene Nanohybrids for High-Performance Flexible Biosensors," *ACS (American Chemical Society) Nano* **4(5):** 2910-2918 (May 2010).

L. Xie, S. G. Chou, A. Pande, J. Pande, J. Zhang, M. S. Dresselhaus, J. Kong, and Z. Liu , "Single-Walled Carbon Nanotubes Probing the Denaturation of Lysozyme," *Journal of Physical Chemistry C* **114(17):** 7717-7720 (May 2010).

Y-P. Hsieh, M. Hofmann, H. Farhat, E. B. Barros, M. Kalbac, J. Kong, C-T. Liang, Y-F. Chen, and M. S. Dresselhaus, "Chiral Angle Dependence of Resonance Window Widths in (2n+m) Families of Single-Walled Carbon Nanotubes," *Applied Physics Letters* **96(10):** 103118 1-3 (March 2010).

J. Kim, H. Xiong, M. Hofmann, J. Kong, and S. Amemiya, "Scanning Electrochemical Microscopy of Individual Single-Walled Carbon Nanotubes," *Analytical Chemistry* **82(5):** 1605-1607 (March 2010).

X. Ling, L. Xie, Y. Fang, H. Xu, H. Zhang, J. Kong, M. S. Dresselhaus, J. Zhang, and Z. Liu, "Can Graphene Be Used As a Substrate for Raman Enhancement?" *Nano Letters* **10(2):** 553-561 (February 2010).

S. Thiele, A. Reina, P. Healey, J. Kedzierski, P. Wyatt, P-L. Hsu, C. Keast, J. Schaefer, and J. Kong, "Engineering Polycrystalline Ni Films to Improve Thickness Uniformity of the Chemical-Vapor-Deposition-Grown Graphene Films," *Nanotechnology* **21(1):** 015601 1-8 (January 2010).

K. M. Milaninia, M. A. Baldo, A. Reina, and J. Kong, "All Graphene Electromechanical Switch Fabricated by Chemical Vapor Deposition," *Applied Physics Letters* **95(18):** 183105 1-3 (November 2009).

M. Kalbac, H. Farhat, L. Kavan, J. Kong, K-I. Sasaki, R. Saito, and M. S. Dresselhaus, "Electrochemical Charging of Individual Single-Walled Carbon Nanotubes," *ACS Nano* **3(8):** 2320-2328 (August 2009).

X. Jia, J. Campos-Delgado, E. E. Gracia-Espino, M. Hofmann, H. Muramatsu, Y. A. Kim, T. Hayashi, M. Endo, J. Kong, M. Terrones, and M. S. Dresselhaus, "Loop Formation in Graphitic Nanoribbon Edges Using Furnace Heating or Joule Heating," *Journal of Vacuum Science and Technology B: Microelectronics and Nanometer Structures* **27(4):** 1996-2002 (July 2009).

S-J. Tsai, M. Hofmann, M. Hallock, E. Ada, J. Kong, and M. Ellenbecker, "Characterization and Evaluation of Nanoparticle Release During the Synthesis of Single-Walled and Multiwalled Carbon Nanotubes by Chemical Vapor Deposition," *Environmental Science and Technology* **43(15):** 6017-6023 (August 2009).

J. Kedzierski, P-L. Hsu, A. Reina, J. Kong, P. Healey, P. Wyatt, and C. Keast, "Graphene-on-Insulator Transistors Made Using C on Ni Chemical-Vapor Deposition," *IEEE Electron Device Letters* **30(7):** 745-747 (July 2009).

L. C. Campos, V. R. Manfrinato, J. D. Sanchez-Yamagishi, J. Kong, and P. Jarillo-Herrero, "Anisotropic Etching and Nanoribbon Formation in Single-Layer Graphene," *Nano Letters* **9(7):** 2600-2604 (July 2009).

A. Reina, S. Thiele, X. Jia, S. Bhaviripudi, M. S. Dresselhaus, J. A. Schaefer, and J. Kong, "Growth of Large-Area Single- and Bi-Layer Graphene by Controlled Carbon Precipitation on Polycrystalline Ni Surfaces," *Nano Research* **2(6):** 509-516 (June 2009).

Meeting Papers

X. Chen, K-J. Lee, D. Akinwande, G. F. Close, S. Yasuda, B. Paul, S. Fujita, J. Kong, and H-S. P. Wong, "High-Speed Graphene Interconnects Monolithically Integrated With CMOS Ring Oscillators Operating at 1.3GHz," Technical Digest (Proceedings), 55th International Electron Devices Meeting (IEDM), Baltimore, Maryland, December 7-9, 2009, pp. 23.6.1 - 23.6.4.

Theses

H. Farhat, *Raman Spectroscopy of Metallic Single Walled Carbon Nanotubes*, Ph.D. diss., Department of Materials Science and Engineering, MIT, May 2010.

A. Reina, *Single- and Few-Layer Graphene by Ambient Pressure Chemical Vapor Deposition on Nickel*, Ph.D. diss., Department of Materials Science and Engineering, MIT, May 2010.

D. A. Nezich, *Fabrication and Electrical Characterization of Transistors Made From Carbon Nanotubes and Graphene*, Ph.D. diss. (co-supervised with Prof. Millile Dresselhaus), Department of Physics, MIT, May 2010.